Final Report WY-20/04F

Field Testing and Long-Term Monitoring of Selected High-Mast Lighting Towers

Jason B. Lloyd, PhD, PE
Robert J. Connor, PhD, PE
Lyles School of Civil Engineering, Purdue University
550 Stadium Mall Dr., West Lafayette, IN 47907
Phone: (208) 421-4471, lloyd1@purdue.edu
Phone: (765) 496-8272, rconnor@purdue.edu

Ryan J. Sherman, PhD, PE
School of Civil and Environmental Engineering, Georgia Tech
790 Atlantic Dr. NW, Atlanta, GA 30332
Phone: (404) 894-2227, ryan.sherman@ce.gatech.edu

Notice

This document is disseminated under the sponsorship of the Wyoming Department of Transportation (WYDOT) in the interest of information exchange. WYDOT assumes no liability for the use of the information contained in this document.

The content of this report reflects the views of the author(s) who are responsible for the facts and accuracy of the data presented herein. The content does not necessarily reflect the official views or policies of WYDOT. This report does not constitute a standard, specification, or regulation.

The State of Wyoming does not endorse products or manufacturers. Trademarks or manufacturers' names appear in this report only because they are considered essential to the objectives of the document.

Quality Assurance Statement

WYDOT provides high-quality information to serve state, industry, and the public in a manner that promotes public understanding. Standards and policies are used to ensure and maximize the quality, objectivity, utility, and integrity of its information. WYDOT periodically reviews quality issues and adjusts its programs and processes to ensure continuous quality improvement.

Copyright

No copyrighted material, except that which falls under the "fair use" clause, may be incorporated into a report without permission from the copyright owner, if the copyright owner requires such. Prior use of the material in a WYDOT or governmental publication does not necessarily constitute permission to use it in a later publication.

- Courtesy – Acknowledgment or credit will be given by footnote, bibliographic reference, or a statement in the text for use of material contributed or assistance provided, even when a copyright notice is not applicable.
- Caveat for Unpublished Work – Some material may be protected under common law or equity even though no copyright notice is displayed on the material. Credit will be given and permission will be obtained as appropriate.

·Proprietary Information – To avoid restrictions on the availability of reports, proprietary information will not be included in reports, unless it is critical to the understanding of a report and prior approval is received from WYDOT. Reports containing such proprietary information will contain a statement on the Technical Report Documentation Page restricting availability of the report.

Creative Commons

1. Report No. WY-20/04F	2. Government Accession No.	3. Recipient's Catalog No.
4. Field Testing and Long-Term Monitoring of Selected High-Mast Lighting Towers		5. Report Date March 2020
		6. Performing Organization Code:
7. Author(s) Jason B. Lloyd, PhD, PE, 0000-0001-8792-3278 Robert J. Connor, PhD, PE, 0000-0002-6964-3317 Ryan J. Sherman, PhD, PE, 0000-0001-7525-4775		8. Performing Organization Report No.
9. Performing Organization Name and Address Lyles Department of Civil Engineering Purdue University 550 Stadium Mall Drive, West Lafayette, IN 47907		10. Work Unit No.
		11. Contract or Grant No. RS07217
12. Sponsoring Agency Name and Address Wyoming Department of Transportation 5300 Bishop Blvd. Cheyenne, WY 82009-3340 WYDOT Research Center (307) 777-4182		13. Type of Report and Period Final Report 4/1/2017 – 3/31/2020
		14. Sponsoring Agency Code
15. Supplementary Notes		

16. Abstract

Four high-mast lighting towers (HMLTs) were instrumented with sensors to monitor weather and structural response to wind-induced vibrations. The four HMLTs were in different locales within the state of Wyoming, each site being selected specifically due to a history of failed HMLTs at those locations, or nearby. Several HMLTs have failed in recent years, some catastrophically, within Wyoming from fatigue crack growth at the base plate-to-tube wall welds. Hence the motivation for the study. Amateur video and some limited data from previous research both supported the possibility that large-amplitude mode I vibration events could be causing the premature fatigue failures. In some cases it was surmised that ice accumulation on an HMLT could be contributing to changes in the aerodynamic response to varying wind events. The research team remotely monitored the four HMLTs with wind-based and stress-based triggers recording data of ambient weather conditions and the aerodynamic response of the HMLTs. The monitoring was carried out continuously for over two years. The instrumentation included an ice sensor capable of detecting the presence of ice, wind speed, wind direction, temperature, and strain. This way, the research team would be able to determine what the structural response to the large-amplitude events would be and if the build-up of ice could be correlated to its occurrence.

Three large-amplitude events were recorded during the two years of field monitoring. Extreme stress ranges were observed during all three events, but particularly in the longest-lasting of the three, reaching peak stresses of up to 40 ksi (ranges of up to 78 ksi) and lasting tens of minutes, effectively consuming between 40 percent and 70 percent of the fatigue life in a single occurrence. The extreme events were found to be relatively rare and unpredictable in terms of when they might transpire.

17. Key Words High mast lighting tower, fatigue, vibration, wind, lock-in, Wyoming	18. Distribution Statement No restrictions. This document is available through the National Transportation Library and the Wyoming State Library.

19. Security Classif. (of this report) Unclassified	20. Security Classif. (of this page) Unclassified	21. No. of Pages	22. Price

SI* (MODERN METRIC) CONVERSION FACTORS

APPROXIMATE CONVERSIONS TO SI UNITS

Symbol	When You Know	Multiply By	To Find	Symbol
		LENGTH		
in	inches	25.4	millimeters	mm
ft	feet	0.305	meters	m
yd	yards	0.914	meters	m
mi	miles	1.61	kilometers	km
		AREA		
in^2	square inches	645.2	square millimeters	mm^2
ft^2	square feet	0.093	square meters	m^2
yd^2	square yard	0.836	square meters	m^2
ac	acres	0.405	hectares	ha
mi^2	square miles	2.59	square kilometers	km^2
		VOLUME		
fl oz	fluid ounces	29.57	milliliters	mL
gal	gallons	3.785	liters	L
ft^3	cubic feet	0.028	cubic meters	m^3
yd^3	cubic yards	0.765	cubic meters	m^3
		NOTE: volumes greater than 1000 L shall be shown in m^3		
		MASS		
oz	ounces	28.35	grams	g
lb	pounds	0.454	kilograms	kg
T	short tons (2000 lb)	0.907	megagrams (or "metric ton")	Mg (or "t")
		TEMPERATURE (exact degrees)		
^oF	Fahrenheit	5 (F-32)/9 or (F-32)/1.8	Celsius	^oC
		ILLUMINATION		
fc	foot-candles	10.76	lux	lx
fl	foot-Lamberts	3.426	$candela/m^2$	cd/m^2
		FORCE and PRESSURE or STRESS		
lbf	poundforce	4.45	newtons	N
lbf/in^2	poundforce per square inch	6.89	kilopascals	kPa

APPROXIMATE CONVERSIONS FROM SI UNITS

Symbol	When You Know	Multiply By	To Find	Symbol
		LENGTH		
mm	millimeters	0.039	inches	in
m	meters	3.28	feet	ft
m	meters	1.09	yards	yd
km	kilometers	0.621	miles	mi
		AREA		
mm^2	square millimeters	0.0016	square inches	in^2
m^2	square meters	10.764	square feet	ft^2
m^2	square meters	1.195	square yards	yd^2
ha	hectares	2.47	acres	ac
km^2	square kilometers	0.386	square miles	mi^2
		VOLUME		
mL	milliliters	0.034	fluid ounces	fl oz
L	liters	0.264	gallons	gal
m^3	cubic meters	35.314	cubic feet	ft^3
m^3	cubic meters	1.307	cubic yards	yd^3
		MASS		
g	grams	0.035	ounces	oz
kg	kilograms	2.202	pounds	lb
Mg (or "t")	megagrams (or "metric ton")	1.103	short tons (2000 lb)	T
		TEMPERATURE (exact degrees)		
^oC	Celsius	1.8C+32	Fahrenheit	^oF
		ILLUMINATION		
lx	lux	0.0929	foot-candles	fc
cd/m^2	$candela/m^2$	0.2919	foot-Lamberts	fl
		FORCE and PRESSURE or STRESS		
N	newtons	0.225	poundforce	lbf
kPa	kilopascals	0.145	poundforce per square inch	lbf/in^2

TABLE OF CONTENTS

LIST OF FIGURES

LIST OF TABLES

EXECUTIVE SUMMARY

Four high-mast lighting towers (HMLTs) were instrumented with sensors and remote data acquisition systems to monitor weather and structural response to wind-induced vibrations. The four HMLTs were chosen in different locales within the state of Wyoming, each site being selected specifically due to a history of failed HMLTs at those locations, or nearby. Several HMLTs have failed in recent years, some catastrophically, within Wyoming from fatigue crack growth at the base plate-to-tube wall welds. Hence the motivation for the study. Amateur video and some limited data from previous research both supported the possibility that large-amplitude mode I vibration events could be causing the premature fatigue failures. In some cases it was surmised that ice accumulation on an HMLT could be contributing to changes in the aerodynamic response to random wind events. Prior to monitoring, each HMLT was pluck tested by the research team recording data and characterizing the dynamic properties of each HMLT. The research team then remotely monitored the four HMLTs with wind-based and stress-based triggers programmed into the data acquisition systems recording data of ambient weather conditions and the aerodynamic response of the HMLTs. The monitoring was carried out continuous for over two years. The instrumentation included an ice sensor capable of detecting the presence of ice, wind speed, wind direction, temperature, and strain. This way, the research team would be able to determine what the structural response to the large-amplitude events were and if the build-up of ice could be correlated to its occurrence.

Three large-amplitude events were observed during the two years of field monitoring. Extreme stress ranges were recorded during all three events, but particularly in the longest-lasting of the three, reaching peak stresses of up to 40 ksi (ranges of up to 78 ksi) and lasting tens of minutes, effectively consuming between 40 percent and 70 percent of the fatigue life in a single wind event. The extreme events were found to be relatively rare and unpredictable in terms of when they might transpire. Furthermore, it was found that the large-amplitude vibrations could occur with or without ice present, suggesting that it is the random resonant pairing of HMLT aerodynamic properties and characteristics of the wind that caused such extreme structural response; which may have been affected by the accumulation of ice, but for which ice was not always necessary.

CHAPTER 1. BACKGROUND

PROBLEM STATEMENT & MOTIVATION

Wyoming Department of Transportation (WYDOT) has experienced multiple fatigue failures of high-mast light towers (HMLTs) in recent years, some as early as two to three years into the service life of the tower. On occasion, these fatigue failures have resulted in catastrophic collapse. Climate data, such as wind, temperature, and presence of moisture recorded at weather stations in relatively nearby locations was reported to suggest that there could have been ice or snow accumulation on the towers at the time of the fatigue failures potentially changing the aerodynamic response of the towers. Several amateur videos have also been circulated on the internet displaying extreme amplitude, low-frequency oscillation of HMLTs in several states, typically captured by passing motorists, some of which appeared to occur in warmer temperature where ice could not have played a factor. However, it couldn't be ruled out and the accumulation of empirical evidence supported the idea that ice accumulation on the towers could be changing aerodynamic response, increasing vibration amplitude, and therefore, fatigue stress range. Previous research by others suggested that very large stress ranges can occur at the tube wall to base plate weld, particular if in addition to large amplitude vibrations the anchor nuts are not tightened properly. Due to the cubed root relationship of stress range to fatigue loading cycles, it stood to reason that this was a possible factor in the premature fatigue failures. Furthermore, it is worth noting that all fatigue failures of HMLTs in Wyoming have been hot-dipped galvanized poles. Cracking of HMLTs during galvanizing due to extreme distortion or liquid metal assisted cracking (LMAC) has been previously researched and is discussed briefly in the literature review.

This report presents the findings and conclusions of a two-year field monitoring project aimed at capturing the rare loading event of large-amplitude mode I vibration of 120-ft tall high-mast lighting towers.

OBJECTIVES

The primary objective of the present research was to record data for large-amplitude mode I vibrations of high-mast lighting towers induced by natural wind events. The challenge with this objective is that the events are random and unpredictable. A secondary and related objective was to determine if there was a correlation between an accumulation of ice on the HMLT and the occurrences; meaning did the large-amplitude lock-in events only occur when there was ice built up on the HMLT. Thirdly, this study set out to understand the behavior of the HMLTs during such events, most importantly the stress ranges at the base plate-to-tube wall welds caused by the large-amplitude displacements.

LITERATURE REVIEW

Nasouri, R., Nguyen, K., Montoya, A., Matamoros, A., Bennett, C., and Li, J. (2019a)

This study focused on the development of a finite element model to simulate the hot dip galvanizing process of high mast lighting towers (or high mast illumination poles) to observe the thermal and mechanical response of these structures. The model replicated the response of the structure going from ambient temperature to the molten zinc bath and then returning to ambient temperatures for cooling. The model was capable of accounting for temperature-dependent material properties, inelastic behavior, large deformation, and contact between metallic components. The model was calibrated using experimental data published by Kleineck (2011) and modeled the Texas Department of Transportation standard detail for welding the tube to the base plate using an exterior collar with full penetration welds and interior seal welds.

The study concluded that the most critical stage of hot dip galvanizing occurs during the dipping step of the process when the tower is partially submerged. The highest mechanical variable response (Von Mises stress and equivalent plastic strain) was found to always be at the bend locations of the tube wall. While the dipping step was found to be most critical, equivalent plastic strain, results indicated that the cooling stage can also produce these critical responses.

Nasouri, R., Nguyen, K., Montoya, A., Matamoros, A., Bennett, C., and Li, J. (2019b)

This study used the finite element model developed by Nasouri et al. (2019a) to conduct a parametric study investigating the effects of pole shape and galvanizing practices on the temperature-induced critical stress and strain demands on high mast lighting towers (or high mast illumination poles) during hot dip galvanizing. The steel material used in the model had nonlinear stress-strain behavior with isotropic hardening and temperature-dependent thermal and mechanical properties.

The analysis concluded that minor changes in the pole geometry, as well as in the galvanizing practices, could help reduce the likelihood of weld toe cracking during galvanizing. The authors determined that the plate-to-pole thickness ratio had significant effect on the potential for galvanization cracking. In models of 12-sided poles, strain demands decreased with a decrease in the plate-to-pole thickness ratio, meaning that the base plate should be thinned or the pole thickened. However, they also note that this is in direct contrast with recommended practices for reducing in-service fatigue demands at the same welded detail, such as reported by Connor and Hodgson (2006). This study further showed that the greatest stress and strain demands were greatest for the 12-sided pole with a base plate thickness of 3.5 inches, which also had the largest base plate to pole thickness ratio, 11. The smallest stress and strain demands were observed for the same pole thickness with the thinnest base plate, having the smallest base plate to pole thickness ratio, 2. Furthermore, this study concluded that using round poles reduced likelihood of cracking as much as reducing the base plate to pole thickness ratio. Consistent with this observation, they also concluded that the stress and strain demands could be reduced on the multi-sided pole by increasing the bend radii. For instance, the authors concluded that increasing the bend radius from 3t (t is the tube thickness) to 14t reduced von Mises stress by 18 percent. The study also concluded that some galvanizing practices could be implemented to help reduce

distortion-induced demands on the pole, such as reducing the dipping time and increasing the dipping angle as much as practicable, and finally adjusting the immersion orientation relative to the axis of the pole such that one of the bends is located at the lowest point was found to also notably reduce equivalent plastic strain demands.

Bellivanis, K. V. (2014)

This study set out to determine if the remaining fatigue life could be estimated for a pole in service with known existing fatigue cracks. It included experimental and analytical studies to accomplish these objectives. Researchers concluded that stress concentration factors at the weld toes near bends of the tube wall were found to be approximately 3 times that of the flats. Also, two methods of remaining fatigue life estimation were in agreement for cracked poles in service, evidence of galvanizing cracking was observed during destructive evaluation of some specimens (further supporting previous research by Kleineck, 2011), and that NDT results can be impeded by the galvanization thickness in combination with weld geometry which can obscure the presence of a crack.

Connor, R. J., Collicott, S. H., DeSchepper, A. M., Sherman, R. J., & Ocampo, J. A. (2012)

The primary objective of NCHPR Project 10-74 was to improve the reliability of HMLTs. The approach included developing loading and analysis criteria for use in the fatigue design of HMLTs, developing a design methodology and specifications with associated commentary for design of HMLTs, and preparing recommended revisions to the existing AASHTO Standard Specifications for Structural Supports for Highway Signs, Luminaries, and Traffic Signals. The research is detailed in NCHRP Report 718 and summarized in Sherman and Connor (2019).

To accomplish the abovementioned objectives, the researchers performed long-term field monitoring on 11 HMLTs ranging in height of 100 to 160 ft with taper rate of 0.14 incher per ft. They pluck tested an additional 15 HMLTs for dynamical properties. All poles included in long-term monitoring were multi-sided with exception of one circular pole. The poles were monitored over the course of two years. Wind speed data and stress-range histogram data were compiled for each location, forming the basis for the proposed fatigue design loads. In addition, Connor et al. (2011) developed recommended damping ratios for Mode I, Mode II, and Mode III vibration, and determined that mitigation of vortex shedding using double-wrap rope strake reduces the number of accumulated cycles without affecting the effective stress range. They also determined that while infinite life design is appropriate, the lifetime loading cycles for HMLTs exceeds the limiting number of cycles at the constant-amplitude fatigue limit state for the most common fatigue detail (Category E) located at the pole-base plate weld. Additionally, they developed static pressure range values for fatigue evaluation of HMLTs, recommended stress range cycle frequencies for fatigue evaluation of HMLTs, and finally concluded that poles with a vertex toward the prevailing wind are more prone to “lock-in”. Lock-in is the term that describes the phenomenon in which the vortex shedding frequency and the structural natural frequency lock-in with one another resulting in large across-wind vibrations.

During the research a video surfaced on the web showing large amplitude oscillations of a HMLT outside Watertown, SD. The HMLT was not being monitored, so no data were available

for the event and it was reported that the pole was removed from service following the event due to cracking. It appeared to have occurred during a late winter storm. This motivated the researchers to comb their data looking for similar events that might have been captured for monitored poles. They found two incidents, one at Creston Junction, WY, and the other at Rapid City, SD. Both cases experienced sustained mode I oscillations of around 10 ksi stress range with sustained winds of about 30 mph. The movement was reported as across-wind.

Kleineck, J. R. (2011)

Following reported collapses of high mast lighting towers around the country, Texas Department of Transportation (TxDOT) initiated an ultrasonic inspection program of their lighting tower inventory, which reportedly revealed many poles in service with fatigue cracks. Following the inspection program, TxDOT initiated a three-part study that included experimental fatigue testing of large-scale specimens with corresponding analytical studies, investigating cracking during the hot dip galvanizing process, and field testing to characterize cracking of poles due to in-service fatigue loading. Kleineck (2011) conducted the study of cracking during hot dip galvanizing of high mast illumination poles. This study was prompted by discovery of cracking in laboratory specimen from the first phase of the three-part study during which researchers discovered that the hot dip galvanized (HDG) specimen had cracked prior to testing.

The research team used full-scale and analytical tests to study the impact of thermal straining after concluding that chemistry, bend radius, and shaft to base plate thickness had minor effects. The researchers instrumented specimens with thermocouples and strain gages gathering data on the temperature and initial strain gradients that occur during dipping into the hot zinc bath. They used this data to calibrate the finite element analysis based parametric study concluding galvanization cracking was generally observed at the toe of the shaft-to-base plate welds concentrated at the bends of the shaft and that for higher diameter-to-thickness ratios, steeper dip angles (8° vs 4°) and quicker dipping speeds will reduce the thermal straining effect. Also, they concluded that reducing the shaft diameter to thickness ratio to below 75 (with 70 recommended) reduces the likelihood of cracking during galvanizing

Magenes, L. (2011)

Magenes (2011) performed the field testing phase of the three-part study funded by TxDOT with the objective to correlate wind speed and direction to stress ranges in the tube wall in order to better understand their fatigue performance. Several poles around Texas were instrumented, with size ranges approximating the HMLTs instrumented for the current research within Wyoming.

This study concluded that vortex shedding occurs at a wind speed close to 7 mph, exciting the second natural mode of vibration – noting that the Texas HMLT has a higher taper rate than most poles helping to reduce vortex shedding. This study further concluded that the effective fatigue stress range (or the equivalent constant amplitude stress range) for all locations studied was close to 1 ksi noting that both vortex shedding and buffeting contribute to fatigue damage of the pole-base plate connection detail.

Connor, R. J., & Hodgson, I. C. (2006)

This study had three primary objectives, which were to quantify stresses in critical components of the towers, identify and measure dynamic properties for accurate prediction of tower response, and characterize the wind phenomenon producing fatigue in the towers. The study was subdivided into two phases. The first phase field tested 10 towers, the second phase tested dynamic properties of 2 additional towers. Towers were instrumented with strain gages, accelerometers, as well as anemometers mounted nearby to characterize wind. The study also included some retrofit towers with external steel jackets installed at the baseplate connection.

The study revealed that higher mode vibration damping ratios were measured lower than provided in AASHTO at the time, loose anchor nuts had a notable effect on stresses measured in the tube wall, but did not affect the damping ratios noticeably. Furthermore, tightening of an anchor nut at a location where the leveling nut was not in contact with the base plate induced a localized stress in the tube wall approaching the yield strength of the material. Low fatigue lives were predicted for unretrofit towers, while retrofit towers were evaluated at over 100 years. The study found that the highest stress ranges were caused by buffeting with measurements as high as 17.5 ksi in the unretrofit towers, while vortex shedding was observed for the second mode vibration with stress ranges around 2 ksi. Additionally, finite element analysis found that by thickening the base plate to 3 inches, for towers taller than 100 ft, can notably reduce fatigue stress ranges in the tube wall

CHAPTER 2. RESEARCH APPROACH

FIELD MONITORING PROGRAM

Four high mast lighting towers located in different areas of Wyoming were selected by WYDOT for instrumentation and long-term monitoring. The towers were selected from locations of interest to WYDOT, including areas where previous towers had failed in fatigue prior to this research project. The four locations and the characteristics of each tower are discussed below in detail.

Researchers from the Steel Bridge Research, Inspection, Training, and Engineering (S-BRITE) Center, at Purdue University, instrumented the four towers in the week of September 11, 2017. Details of the field monitoring are discussed in the following, including the instrumentation, sensors, data acquisition, remote communications, and data storage. Typically field testing and fatigue evaluation of structures subject to environmental loads, such as wind, should be tested for a minimum of one year in order to capture all seasonal effects resulting from variable weather patterns. Field testing for this project continued for two years, finishing in October 2019. The additional year of monitoring was performed in an extended effort to capture the relatively rare loading event that causes large amplitude mode I oscillations of the lighting towers.

Overview of Test Sites

All four HMLTs were instrumented during the week of September 11, 2017. Prior to arrival of the Research Team, WYDOT personnel positioned a temporary pole at each location for installation of the anemometer and ice sensor. Details of the sensor installation are discussed in the next section, entitled *Instrumentation*. The four locations of the towers were the Vedauwoo Interchange (District 1), Dwyer Junction (District 2), Baxter Interchange (District 3), and Buffalo Tri-Level (District 4).

Vedauwoo Interchange:

The HMLT monitored in District 1 was positioned on the east side of Interstate 80 at the Vedauwoo exit (Exit 329). Figure 1 shows an image taken from Google Earth where the Vedauwoo Climbing Area access road can be seen intersecting with I-80. The red arrow indicates the location of the HMLT just south of the exit. Figure 2 shows the HMLT from the roadway driving westbound along I-80. The image shows the orange equipment box, which housed the data acquisition system (DAQ), and the temporary pole on which the anemometer and ice sensor were installed. The temporary pole was installed by WYDOT a minimum of 10 ft. from the HMLT to ensure wind measurements were not affected by proximity of the pole.

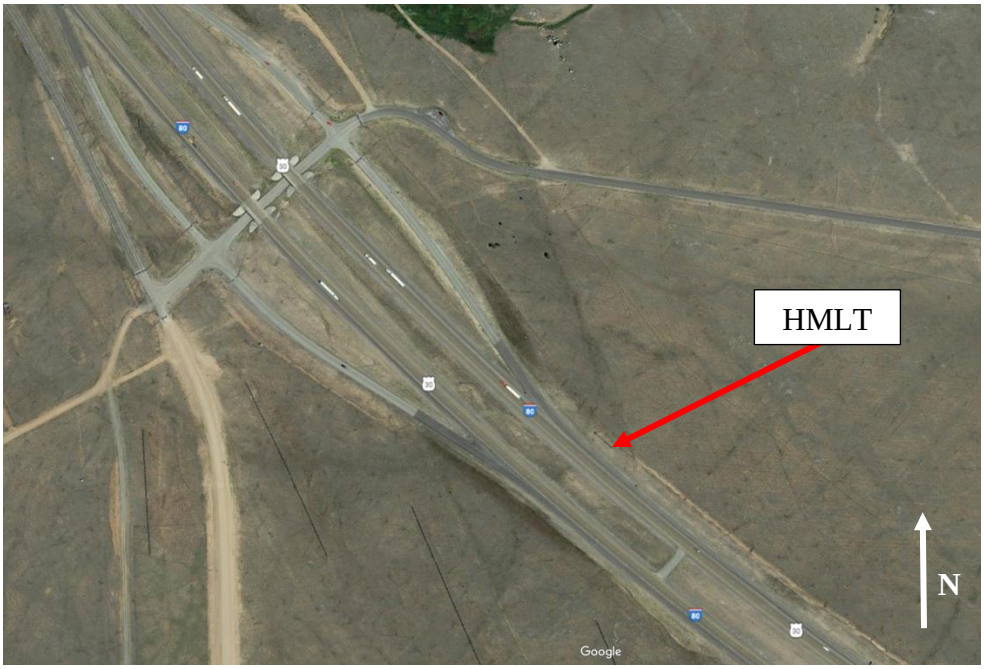

Original Photo: ©2019 Google®

Figure 1. Photo. Location of HMLT tested at the Vedauwoo Interchange.


Original Photo: ©2019 Google®

Figure 2. Photo. Street view of the HMLT at Vedauwoo Interchange.

Dwyer Junction:

The HMLT monitored in District 2 is positioned at the Dwyer Junction rest stop adjacent to the walking path leading to the truck parking area. Figure 3 shows an image taken from Google Earth where the Junction of I-25 and U.S. 26 can be seen. The red arrow indicates the location of the HMLT within the rest stop area. Figure 4 shows the HMLT from the roadway driving into the rest stop area. The image shows the orange equipment box, which housed the data acquisition system (DAQ), and the temporary pole on which the anemometer and ice sensor were installed.

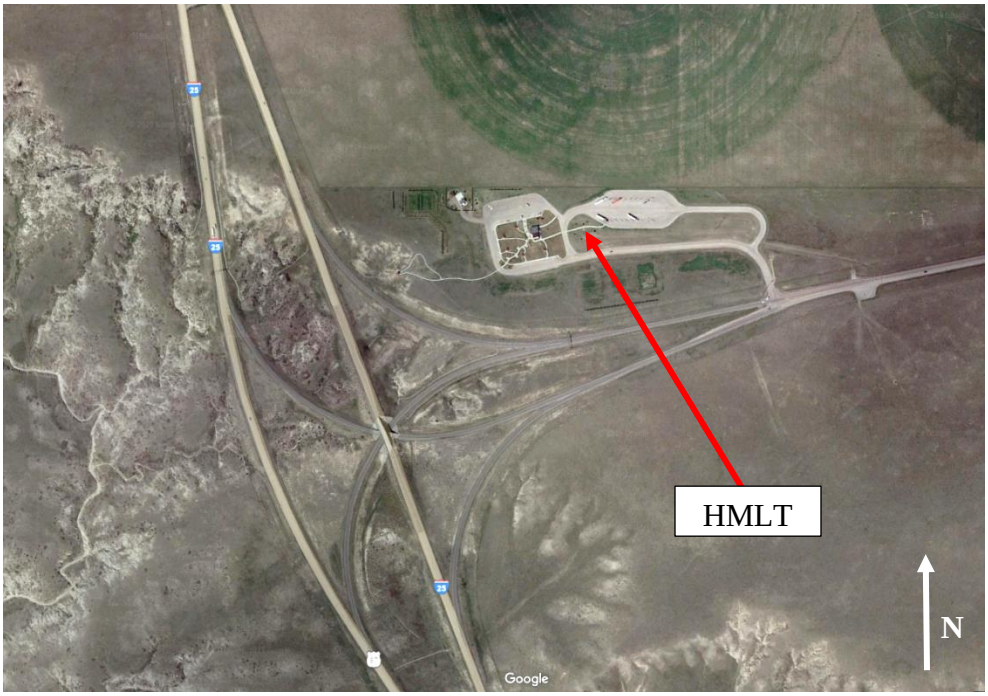

Original Photo: ©2019 Google®

Figure 3. Photo. Location of HMLT tested at Dwyer Junction.

Original Photo: ©2019 Google®

Figure 4. Photo. Street view of the HMLT at Dwyer Junction.

Baxter Interchange:

The HMLT monitored in District 3 is positioned in the median of Interstate 80 at the Baxter Interchange (Exit 111). Figure 5 shows an image taken from Google Earth where State Road 370 can be seen intersecting with I-80. The red arrow indicates the location of the HMLT just west of the exit. Figure 6 shows the HMLT from the roadway driving eastbound along I-80. The image shows the orange equipment box, which housed the data acquisition system (DAQ), and the temporary pole on which the anemometer and ice sensor were installed.

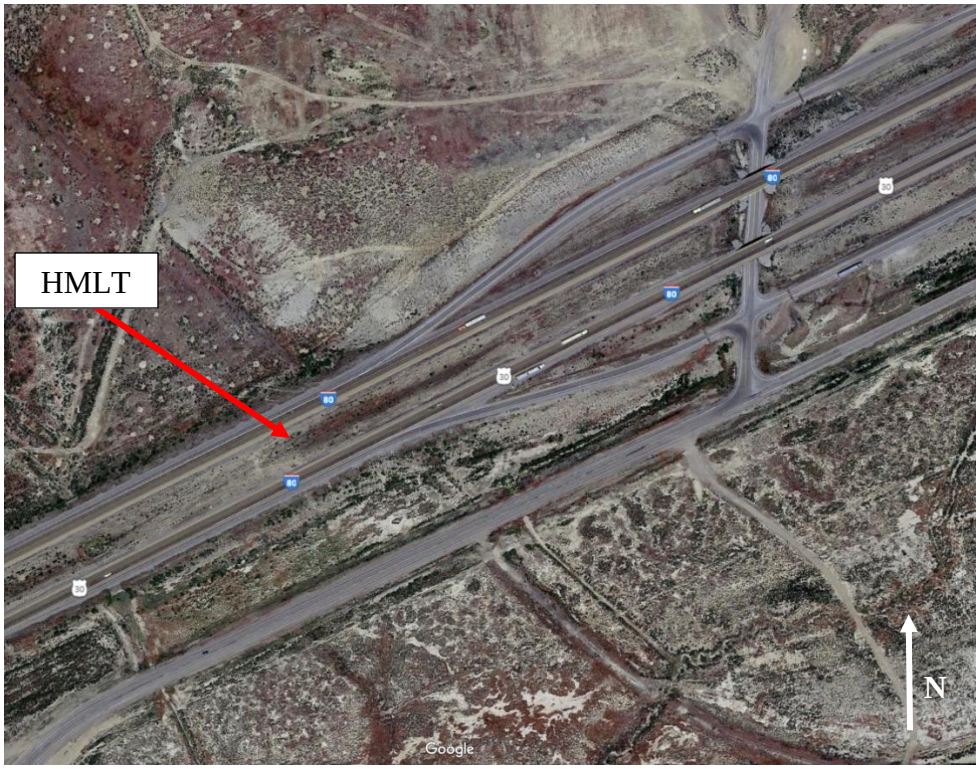

Original Photo: ©2019 Google®

Figure 5. Photo. Location of HMLT tested near Baxter Interchange.

Original Photo: ©2019 Google®

Figure 6. Photo. Street view of the HMLT near Baxter Interchange.

Buffalo Tri-Level:

The HMLT monitored in District 4 is positioned in the median just east of the I-25 on-ramp at the Buffalo Tri-Level interchange of I-90 and I-25. Figure 7 shows an image taken from Google Earth where the entire interchange can be seen. The red arrow indicates the location of the HMLT. Figure 8 shows the HMLT from the roadway driving southbound along the I-25 on-ramp. The image shows the orange equipment box, which housed the data acquisition system (DAQ), and the temporary pole on which the anemometer and ice sensor were installed.

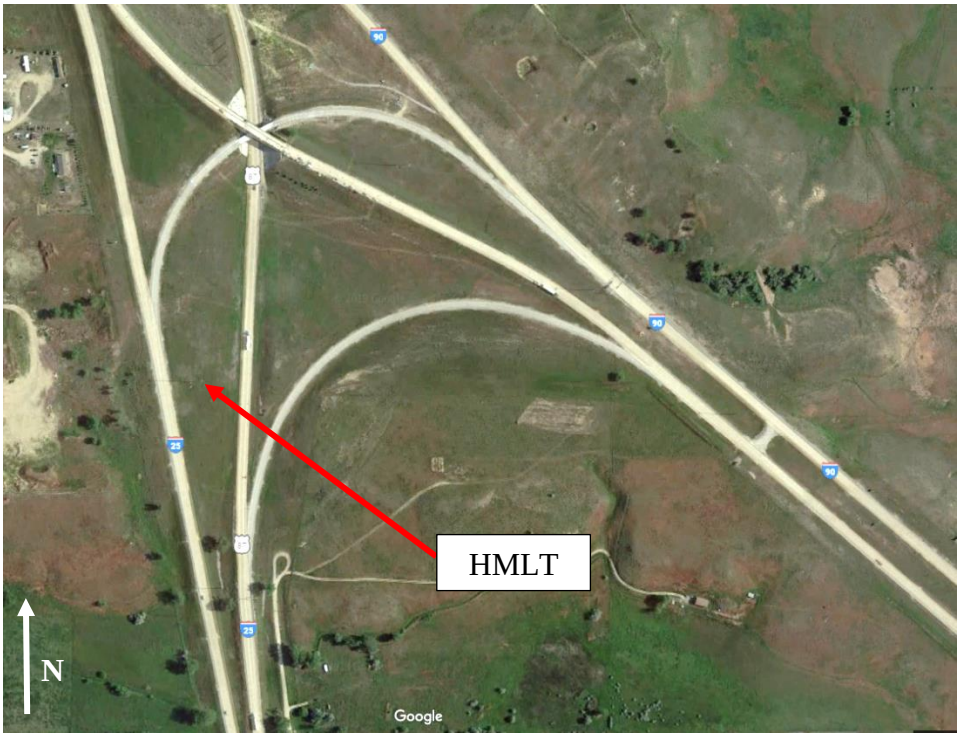

Original Photo: ©2019 Google®

Figure 7. Photo. Location of HMLT tested at Buffalo Tri-Level.

Original Photo: ©2019 Google®

Figure 8. Photo. Street view of the HMLT at Buffalo Tri-Level.

Summary of HMLT Dimensions and Base Weld Detail

The dimensions characterizing each HMLT are summarized below in Table 1. All of the HMLTs shared similar dimensions, with the only exceptions being the base plate thickness and tube base diameter for the Vedauwoo Interchange.

Table 1. Key dimensions for each HMLT.

HMLT	Pole Height (ft)	Tube				Base Plate			Bend Radius-to-Tube Thickness Ratio	Base Plate-to-Tube Thickness Ratio
		Taper (in/ft)	Base Dia. (in)	Thick (base) (in)	No. of Sides (base)	Plate Dia. (in)	Bolt Circle Dia. (in)	Thick (in)		
Vedauwoo Int.	120	0.14	23.28	0.375	16	35	29	2.0	10.6	5.3
Dwyer Junct.	120	0.14	24.25	0.375	16	36	30	2.5	10.6	6.6
Baxter Int.	120	0.14	24.25	0.375	16	36	30	2.5	10.6	6.6
Buffalo Tri	120	0.14	24.25	0.375	16	36	30	2.5	10.6	6.6

The last two columns are noted as a convenience to the reader to compare to research conclusions reported by Nasouri et al. (2019b). Recall that in this study the authors used finite element analysis to carry out a parametric study in order to characterize HMLT characteristics and dipping practices that may help reduce the risk of cracking during hot dip galvanizing. The bend radius-to-tube thickness ratios for these HMLTs monitored as part of this research are toward the high side of the range studied by Nasouri et al., which varied from 3 to 14, with 14 having the most beneficial results. While it cannot be determined with a high level of certainty, this would suggest that the bend radius-to-tube thickness geometry of the Wyoming HMLTs, included in this research should have helped reduce risk of cracking during galvanizing. The base plate-to-tube thickness ratios are approximately mid-range of those studied by Nasouri et al., which ranged from 11 to 2, with 2 having the most beneficial results. Once again, it is difficult to draw a conclusion from this, but it may suggest that there is moderate risk of galvanizing cracking to this geometric relationship.

The weld detail for the base plate-to-tube wall weld is shown in Figure 9. This detail was typical for all monitored HMLTs, as was confirmed in the fabrication shop drawings for each. This detail is different than the typical TxDOT weld detail that was modeled in Nasouri et al. (2019a) and (2019b). The typical TxDOT weld detail for HMLTs also has a full penetration weld, however, it has an external collar (or ring) left in place with seal weld on the interior of the tube wall. This is pointed out only to ensure the reader is aware that while some conclusions from Nasouri et al. (2019a) and (2019b) may have applicability, it is difficult to draw absolute conclusions due to the fact that there are minor differences in the welded detail of primary concern.

Finally, the fatigue category of the tube wall-to-base plate weld shown in Figure 9 is E', as provided in AASHTO *Standard Specifications for Structural Supports for Highway Signs, Luminaires, and Traffic Signals*, Article 11.9.

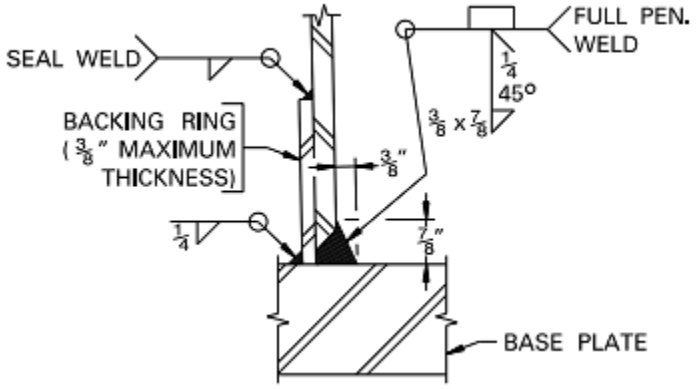

Source: WYDOT Standard Details, Sheet 1 of 3

Figure 9. Base plate-to-tube wall weld detail.

Instrumentation

The Research Team instrumented all HMLTs during the week of Sep 11, 2017. Prior to arrival, WYDOT personnel had installed a separate temporary pole at each location for positioning of the anemometer and ice sensor. An example of this is shown in Figure 10. These poles were all located a minimum of 10' from the HMLT in order to ensure wind patterns were not interrupted by proximity to the HMLT. The installation height varied slightly for each anemometer based on the top elevation of the temporary poles. The industry standard for wind measurement is 33 ft. above the ground, as defined by AASHTO Standard Specifications for Structural Supports for Highway Signs, Luminaires, and Traffic Signals, Article 3.2, *Basic Wind Speed*. Slight variance from the standard 33 ft is not believed to significantly impact the wind data.

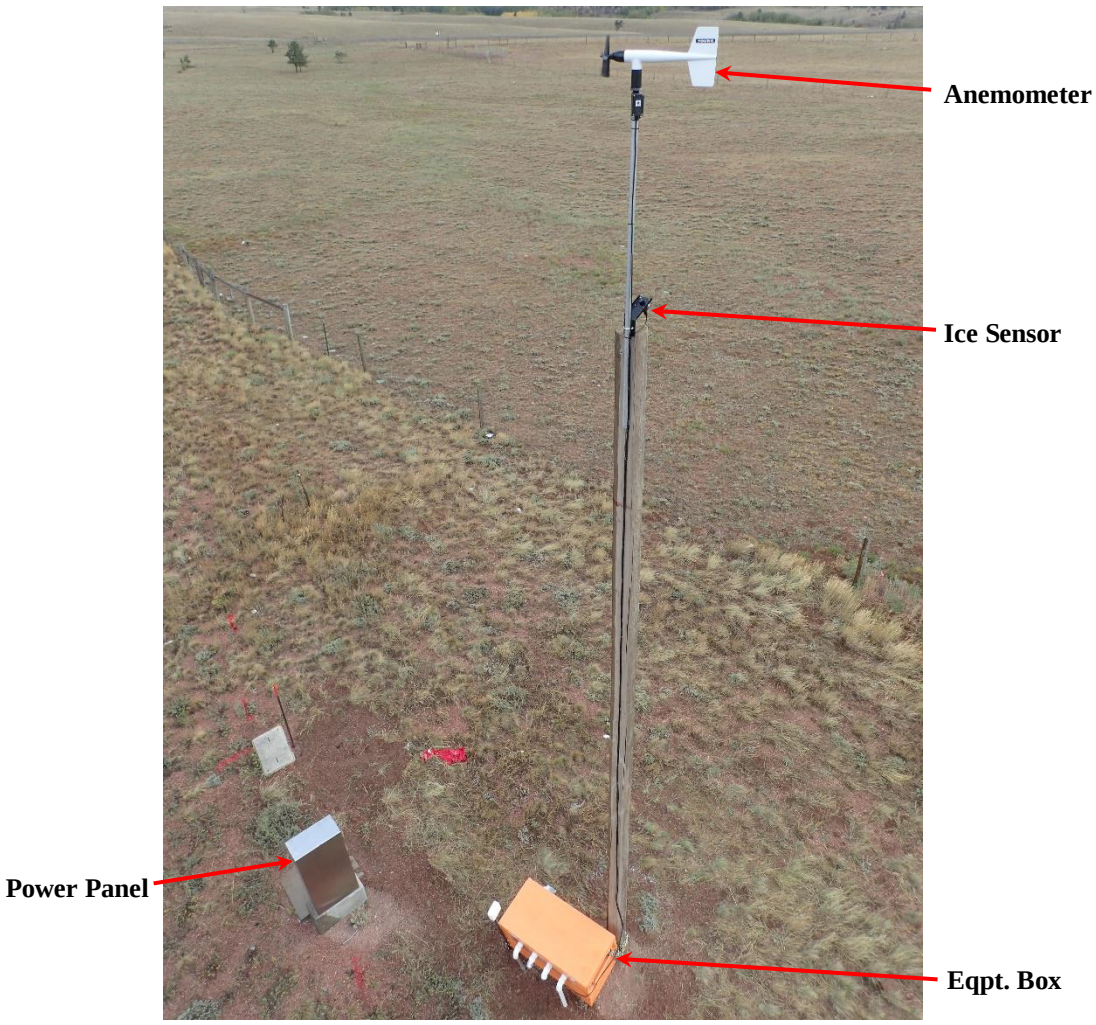

Figure 10. Temporary pole and equipment box

Equipment Box

Extensive measures were taken to protect the equipment during the long term monitoring enabling safe and reliable operation for the duration of testing. The equipment boxes were made from steel job boxes, modified by the Research Team for the purpose of protecting the monitoring and communications equipment from the environment, theft, and vandalism. An example of one is shown in Figure 11. The boxes were outfitted with two layers of insulation to help moderate interior temperatures. Additionally, the boxes were fitted with a ventilation fan and exhaust duct to circulate interior and exterior air when interior temperatures became too warm. This was monitored and controlled using the CR6 Datalogger.

A shelf was built into the box to set the data logger and modem. Below the shelf the battery bank and charging unit were stored. Wire ports were installed at the front enabling penetration of the box for communications and sensor wires while maintaining a seal against weather and rodent entry. Ports were sealed around the wires and cables. Conduit was installed in approximately 6-in deep trenches between the box and either the HMLT or anemometer pole to keep wires out of the reach of lawn mowers and rodents. The conduit was brought out of the ground adjacent to the

HMLT, as seen in Figure 12. The equipment box was fitted with a gasket around the lid to further seal against dust and moisture intrusion, dual locks to prevent unauthorized access, and each was chained to either the HMLT or anemometer pole. Finally, the Research Team placed ant bait and moth balls inside each box in order to mitigate pest intrusion and sealed the lock ports against rain water infiltration.

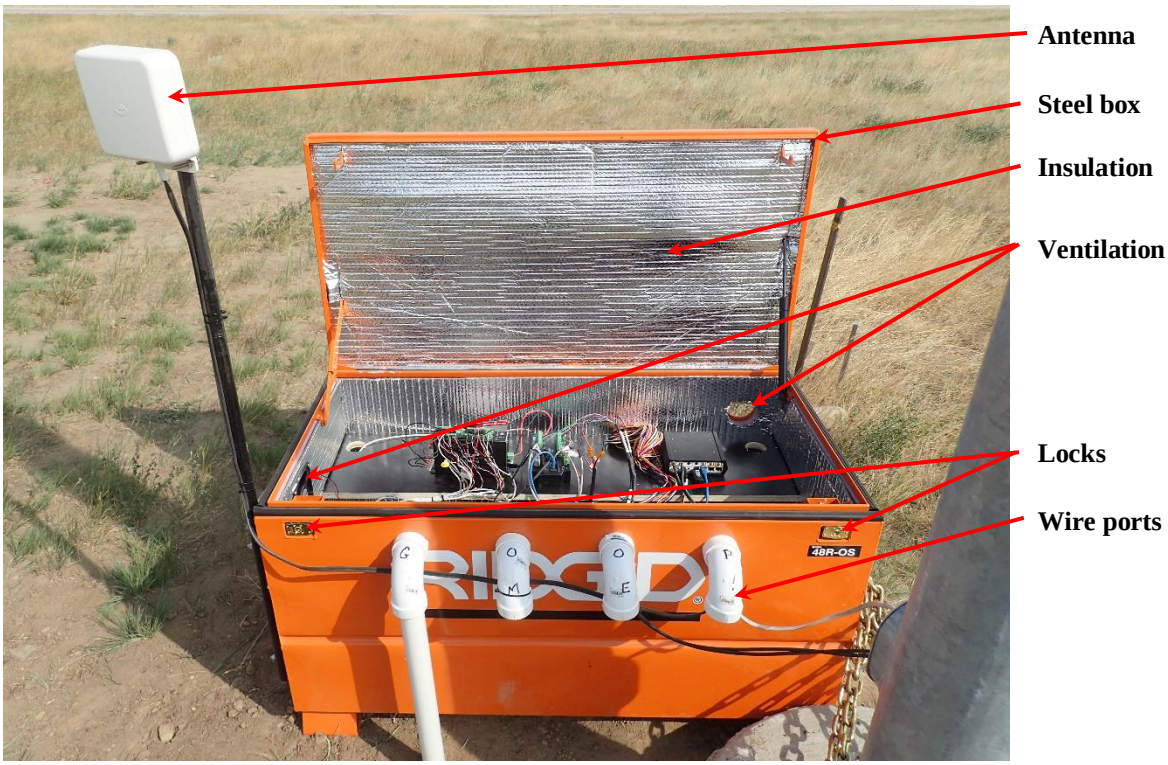

Figure 11. Equipment box

Figure 12. Example of underground conduit used to protect signal wires.

Power Supply

The power supply is shown in Figure 13, which was housed inside the equipment box. The primary power source was local 120VAC power located at the power panel for each HMLT. An extension cord was run underground from the power panel to the interior of the equipment box. The battery charger/maintainer was plugged into the local 120VAC power. A NOCO Genius G15000 12V/24V 15A charger was used. This charger is able to rapidly charge low batteries. It is also equipped with battery maintaining logic allowing it to monitor battery voltage and supply commensurate drip charge to the system, as needed to maintain the battery bank at full charge without overcharging.

Four deep cycle marine batteries were wired in parallel between the battery charger, and the monitoring and communications equipment. The battery bank was wired in parallel making amperage-hours additive in order to maximize backup power to protect against local power outages or brown-outs and maximize DAQ system time of operation. A terminal board was wired into the battery bank, which distributed the required 12VDC power to all of the monitoring and communications equipment. Excitation voltages required for the operation of the sensors were supplied by the data logger. The exception to this was the ice sensor, which required a

24VDC power supply in order to heat the probe tip element and melt any accumulated ice. This power was supplied using a Mean Well HEP-100 AC-DC power supply that was plugged directly into the local 120VAC power cord.

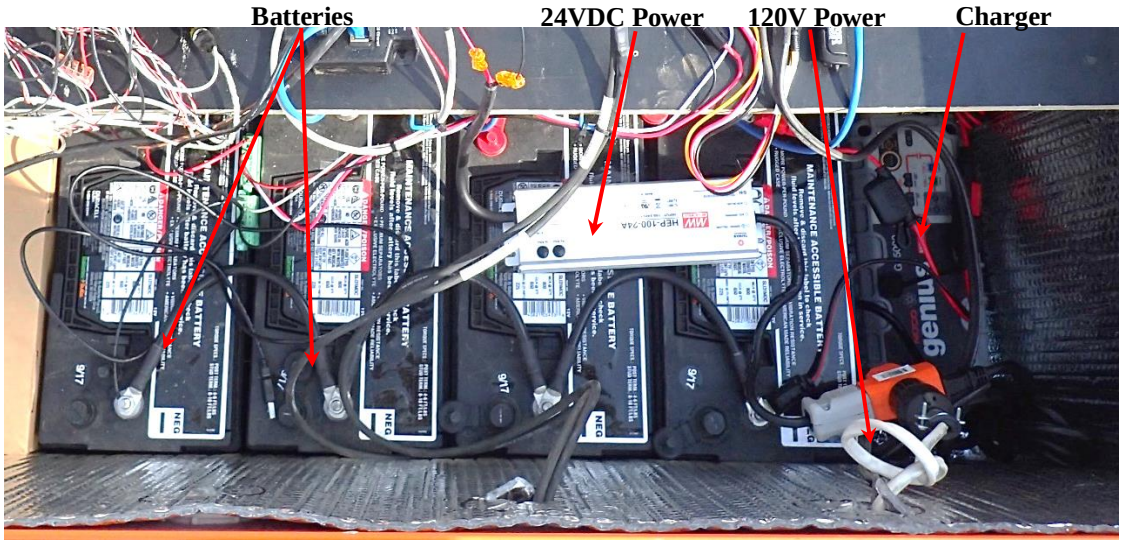

Figure 13. Battery bank power system

Datalogger

The data logger used for pluck tests and long-term monitoring was the Campbell Scientific CR6, seen in Figure 14. The CR6 is a very low power, versatile 24-bit resolution ADC data logger with programmable universal terminals that can be configured for essentially any sensor. The CR6 has an onboard central processing unit (CPU) allowing programming and stand-alone operation. The CR6 is relatively small, but can be expanded using CDM-A116 input modules with capacity for 16 differential channels each. A CR6 and CDM-A116 were used at each site during field testing to sample data from several foil resistance strain gages, the anemometer, ice sensor, thermocouple, and accelerometer. In addition to sampling and recording data, the CR6 also communicated via cellular modem with a remote server housed at Purdue University for data storage, as well as monitored the interior temperature of the equipment enclosure triggering the internal ventilation fan when required to moderate operating temperatures for the equipment and battery bank. Finally, the CR6 monitored the voltage of the battery bank as an indicator of battery health and operation. The CR6 was also furnished with a 2 GB Micro SD card for local data storage. All data sampled and recorded by the data logger and expansion module were saved locally to the micro SD card. Upon link-up with the remote server, the data was copied from the micro SD card and transferred to the server. This provided an additional layer of back up for all data. Data collection and storage is further explained below.

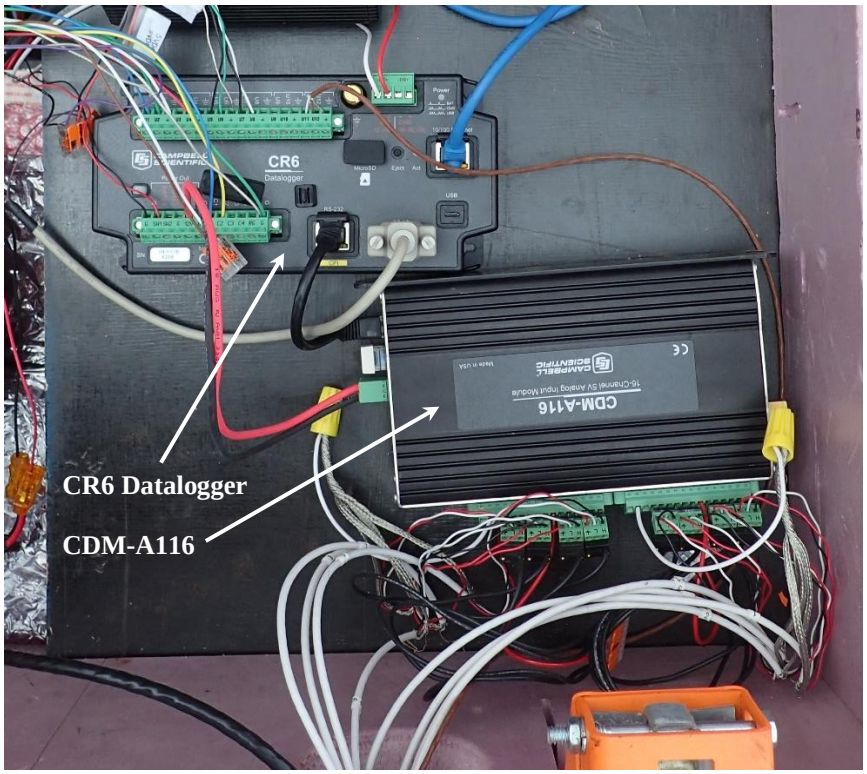

Figure 14. CR6 Datalogger and CDM-A116 Module

Communications

Remote communications with the data logger were achieved via a cellular modem. The CalAmp Fusion Dual Network LTE Router was the modem used. It was setup with a Verizon Wireless data SIM card and was connected to a Dual LTE/4G Yagi directional antenna. Once the modem and antenna were powered on and locally connected to a laptop, the antenna was rotated until the strongest signal was acquired.

Anemometer

The wind monitor used was the Young Model 5103, as can be seen in Figure 15. It is a high performance corrosion-resistant wind speed and direction sensor. The propeller produces an AC sine wave voltage signal whose frequency can be sampled by the data logger and the vane angle (direction of wind) is sensed by a precision potentiometer. Results were returned using a 3 second running average, which is a common averaging time for wind gust measurements, and were converted to speed and angle using calibrated multipliers. All results signify the direction from which the wind is blowing (e.g., 270 degrees would indicate a wind blowing from the west toward the east).

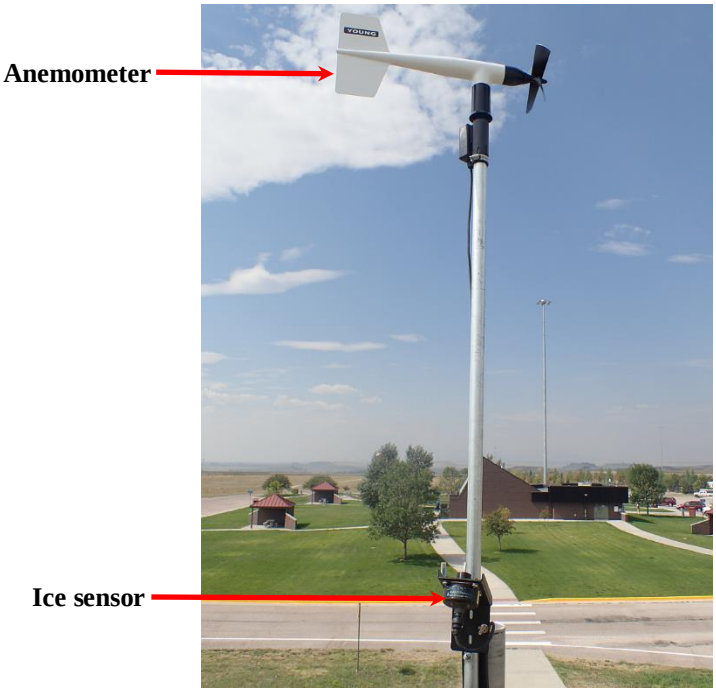

Figure 15. Typical installation of anemometer and ice sensor

Ice Sensor

The freezing rain sensor is made by Rosemount Aerospace, Inc., Model 0871LH1. It detects the presence of icing conditions, or ice accumulation. The installation location can be seen in Figure 15, showing it mounted at the top of the temporary pole, below the anemometer, on the manufacturer-provided mounting bracket. The ice sensor operates using resonant frequencies of a nickel alloy probe. As ice collects on the probe, the added mass causes the resonant frequency to decrease. When the frequency decreases to about 130 Hz (resulting from a layer of ice of about 0.02 inches), the data logger logs an ice event and the ice sensor automatically defrosts the probe, and begins the process again.

Figure 16. Freezing rain sensor and mounting kit

Strain Gage

Stresses in the tube wall were measured using eight weldable, foil resistance strain gages produced by Vishay Micro-Measurements. The gages were model LWK-06-W250B-350 with an active grid length of 0.25 inches, strain range of ±5000 µin, and nominal resistance of 350 ohms. Excitation voltage was five volts. This type of strain gage is a uni-axial, foil resistance type gage that is temperature compensated for use on structural steel and were wired to the data logger in a three-wire configuration in order to cancel out lead wire temperature effects. An example of the installation of the weldable strain gage, prior to application of weather protection, is shown in Figure 17.

The strain gage comes pre-bonded to a steel tab from the manufacturer, making installation simpler, more versatile in poor weather, and less prone to mistakes. To attach them to the structure, several pinprick-size resistance spot welds are made on the steel tab. The spot welds pose no short or long-term concern with respect to stress concentration or fatigue. The surface of the steel girder is first prepared by grinding smooth down to base metal and then cleaning with degreaser agent. Next, the gage is spot welded into place, then the exposed base metal is coated with zinc-rich paint, and finally a weather protection system is installed to guard the gage against the environment.

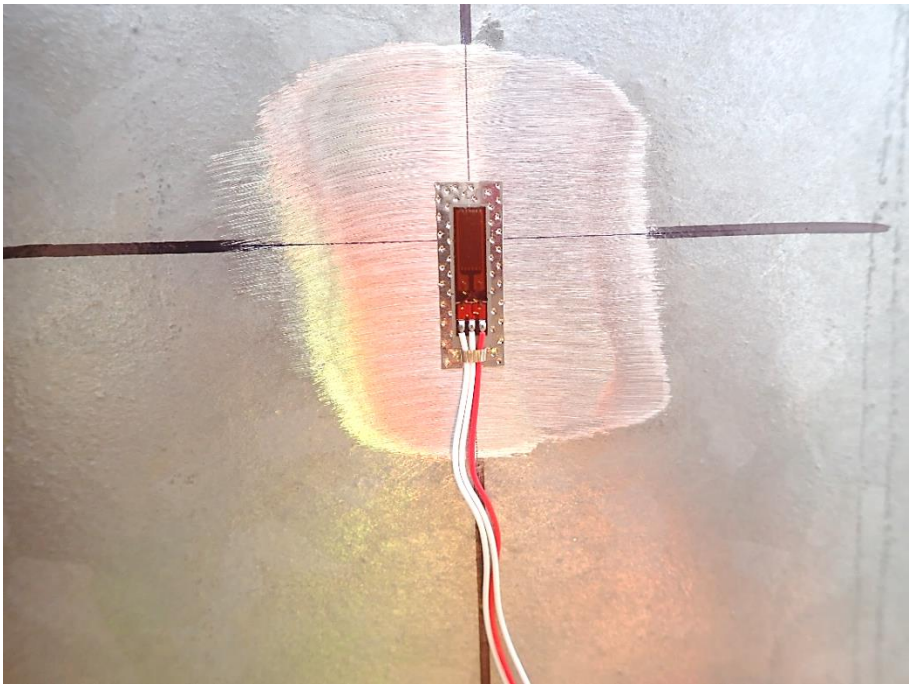

Figure 17. Weldable strain gage

All strain gages were installed seven feet above the top surface of the base plate, providing a distance from the hand hole slightly greater than one and half times the diameter of the HMLT. A single gage was installed on every other tube wall flat, providing nominal stress measurement along all the major axes with a redundant gage for each. Having the measured nominal stress range at a known height on the pole allows the Research Team to validate statics and extrapolate the nominal stresses at the base of the tube near the base plate weld. Figure 18 shows the typical installation of the gages, and Appendix A contains the detailed instrumentation plans for each location monitored. Channel, or gage, 1 was always installed on the flat facing magnetic south.

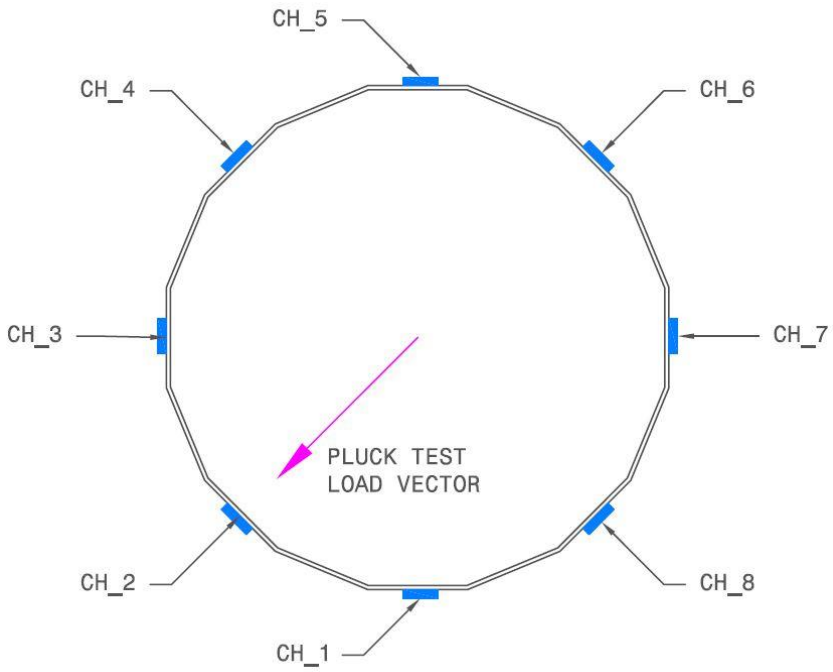

Figure 18. Sketch showing installation of strain gages on tube wall cross-section

Accelerometer

Accelerations were measured during the pluck tests using a bi-axial accelerometer produced by Bridge Diagnostics, Inc., Model BA1521-005, with an excitation voltage of 5 volts. This accelerometer has an acceleration range of ±5g. The accelerometer can be seen in Figure 19 attached to the HMLT using the manufacture-recommended mounting block and stainless steel strapping. The sensors were installed at 30-ft above the top surface of the base plate, facing south, as shown in the instrumentation plans in Appendix A.

Figure 19. Bi-axial accelerometer

Thermocouple

A twisted shielded thermocouple wire produced by Omega, type FF-J-24-TWSH-SLE, was installed on the exterior surface of the HMLT tube wall to collect data on the pole steel surface temperature. This data helped correlate with presence of ice data from the freezing rain sensor to validate potential for presence of ice. The surface temperature is also a good set of data to have if needed to further understand ambient conditions surrounding the HMLT.

Load Cell

An Omega Dyne Model LC111-5k Stainless S-Beam Load Cell was used in line with the plucking strap for the pluck tests. The load cell was calibrated in tension prior to being deployed to the field. A voltage to load unit force multiplier was obtained during the calibration, which was plugged into the data logger program such that real time output on the computer during the testing was pounds.

Figure 20. Omega Dyne Model LC111-5k Stainless S-Beam Load Cell

Data Collection and Storage

There were four different primary types of field test data collected and stored throughout the project, namely, dynamic response (pluck) test data, stress range histogram (using Rainflow algorithm), ambient data, and triggered time-history data.

Pluck Test Data

Data from the pluck tests were measured from the accelerometer and strain gages. The pluck tests were iterated three to four times ensuring repeatability and consistency of the test results. The pluck test data were analyzed to identify modal frequencies of each HMLT using the Fast Fourier Transform (FFT) method.

Stress Range Histogram Data

Stress range histogram data were collected using the Rainflow-counting algorithm. The Rainflow-counting method is used in the processing and analysis of fatigue data in order to reduce the highly variable spectrum of stress resulting from random loading sequences into sets, or bins, of equivalent stress cycles. Stress range histograms are generated from stress time-history records, or a continual sampling of data through time. Stress time-history data records quickly become prohibitively large and unmanageable. Thus, the data logger is programmed to buffer the stress time-history data over a period of time, process it through the Rainflow-counting algorithm generating the histogram, and then discard the buffered data, and begin again. The process captures the equivalent stress cycle history while condensing the information to a manageable amount that can be readily stored and remotely transferred. The period of time over which data were processed into histograms was 10 minutes. This is a typical period used in field testing of bridges and other metal structures and has been found by the authors to provide a conservative, yet accurate, representation of the variable stress spectrum experienced by the structure.

Ambient Data

For the purposes of this research project, ambient data refers to a collection of maximums and averages over a pre-determined period of time for wind speed, wind direction, steel surface temperature, and battery bank voltage. These data provide a snapshot of ambient temperatures and wind characteristics, along with battery bank health, throughout monitoring, which his particularly useful during periods in which triggered time-history data are not being collected.

Triggered Time-History Data

Triggered time-history data were collected using programmed logic that the data logger used to compare sampled data from the sensors to trigger thresholds. If the data value met the criterion of a trigger event, the data logger would record the buffered time-history data leading up to the trigger event, and then a programmed set of data, typically over a desired period of time, following the trigger. Once triggered, the data recorded was a continuous time-history intended to record periods of high wind buffeting. Triggers were based on wind speed, as well as peak stress. Early in the project the wind speed triggers were 30 mph, 40 mph, and 50 mph. Later in the project, after collecting sufficient 30 mph trigger event data, the wind triggers were limited to the higher wind speeds of 40 and 50 mph. Peak stress triggers were also set at ±5 ksi and ±10 ksi in the event that low wind speed buffeting might cause resonant high amplitude oscillations. In each trigger event, data were recorded into unique tables.

Data Backup and Security

Data collection and storage for long-term monitoring was carefully built with multiple layers of security and backup. As data was collected, it was stored locally on the micro SD card in the data logger. The card had sufficient capacity for approximately three months of data at the windiest of the four locations. The data was temporarily stored on the micro SD card in between remote communication linkups with a server at Purdue University. A software produced by Campbell Scientific, Inc., called LoggerNet, was installed on the server. This software has many functions related to data logger support, such as programming, communications, and data retrieval. It has the capacity to manage communications and data retrieval with a network of data loggers simultaneously. It can be used to remotely communicate with a data logger on demand or automatically at a user-defined interval. In this case, LoggerNet was programmed to contact each data logger every 15 minutes and collect all new data since the previous linkup. In the case that remote linkup could not be made at any given interval, the data would remain on the micro SD card at the data logger until communications could be re-established. Over the course of the two years, this occurred occasionally, but not consistently and provided a very reliable communications system. Once the data was retrieved from the data logger it was securely stored on the server. The server was then backed up nightly to backup servers also located at Purdue University. In addition, about every one to two months the data was also manually copied from the primary server by a member of the Research Team and saved to commercially available cloud storage. This means that at any given time the same data could be obtained from three or more servers providing the upmost protection for long-term storage. Data on the micro SD card would remain stored until the card was filled at which point the data logger was programmed to begin to overwrite the oldest of existing data. Thus, the ring memory cycle was generated

helping to ensure data was stored locally for as long as possible enabling any break in remote communications to be restored and no data lost.

The data loggers were constantly monitoring the sensors collecting measurements and processing the values against programming logic. However, data were only kept if a “trigger” was met. A trigger is a user-defined threshold defined within the data logger program that when encountered would prompt the data logger to record a data set to the micro SD card. Generally the data set would consist of many data every second over a set period of time, such as a few seconds leading up to the trigger and several seconds to a few minutes after. Recorded data prior to the trigger event is possible because the data logger, while constantly monitoring, is also temporarily storing the data into a buffer that can be permanently recorded upon trigger, and without a trigger is recorded over. The triggers used and some of the programming logic are described in the following sections.

CHAPTER 3. REVIEW OF FIELD DATA

FIELD TESTING

The field testing program was comprised of a dynamic response test, also referred to as a pluck test, and variable load long-term monitoring. The pluck test was performed for each of the four HMLTs at the time of instrumentation. Following completion of installation and calibration of the sensors, the field team conducted the pluck test in order to collect a benchmark set of data characterizing the dynamic response of each HMLT with a known load. The same sensors and data acquisition system at each site were then used for the long-term monitoring, switching only the data logger program.

Setup for the Dynamic Response (Pluck) Tests

Instrumentation for the pluck tests included strain gages and a biaxial accelerometer. The data logger was programmed with a data sampling rate of 50 Hz, meaning that a data point for each sensor was recorded fifty times per second throughout the test, from start to finish. The data were observed in real time using a laptop computer connected to the data logger.

Figure 21 demonstrates an example of the setup for the pluck test, showing the test at the Buffalo Tri-Level. This reflects the same basic setup used at all testing locations. In this photograph it can be seen that the HMLT has been rigged with a strap. The strap was connected to the HMLT 32 ft. above the top surface of the base plate. In line with the strap were the S-beam load cell, a ratchet strap (come-along), and a quick release. With the strap anchored near the ground, either to a truck or aerial lift, the ratchet strap was used to apply a load to the HMLT between 1,000 – 2,000 pounds. The Research Team used a measuring tape and a laser distance measuring device to measure the horizontal leg of the loading triangle created by the setup. This way the load could be resolved into vertical and horizontal components and the measurements in the strain gages could be checked against theoretical calculations as another check for accuracy. The load vector was along the out-of-plane axis aligned with strain gage 2, pulling about 225 degrees off magnetic north for all of the sites except Vedauwoo, which due to the location of a fence, the load vector was moved to 315 degrees off magnetic north aligned with gage 4.

Figure 21. Pluck testing the HMLT at Buffalo Tri-Level

Once the strap was pulled to between 1,000 and 2,000 lbs, the quick release was triggered exciting a dynamic oscillation in the HMLT as it elastically rebound. Due to the load being applied relatively low on the HMLT, the dynamic response was primarily second or third mode vibrations rather than a large amplitude mode I sway. The magnitude of the load also ensured that the stresses in the HMLT tube wall remained far below yield capacity, generally with peak stress at the strain gage location of the pole being around 2 ksi. Data from the biaxial accelerometer were collected and analyzed to determine dynamic properties of each pole. This is explained further in the following section.

Results of the Dynamic Response (Pluck) Tests

A sample of pluck test data is plotted in Figure 22. The strain measured by strain gages 2 and 6 has been converted to units of stress, ksi, using a calibrated multiplier. The double-y axis chart plots stress along the left vertical axis and load along the right vertical axis. These are plotted relative to time along the horizontal axis. It can be observed that as load increased, approximately equal and opposite stresses developed in the pole at the location of the two strain gages shown. These gages were installed opposite each other on the pole at a position of maximum bending stress. Thus, it would be expected that due to symmetry of the pole the stresses would be approximately equal with opposing signs. In this case, and the case of all stress data collected during this project, a negative sign indicates compression and a positive sign indicates tension. Figure 22 shows that load, and consequently stress, are shown to increase with distinct steps. This is due to the functionality of the ratchet strap used to apply load. Considering this figure again, it can be seen that at just past 200 seconds, the load is quickly released and stress oscillations are seen in the figure dampening out toward zero. Prior to releasing the load,

the HMLT was allowed to dampen to minimize the measured effect of the vibration from the ratcheting process.

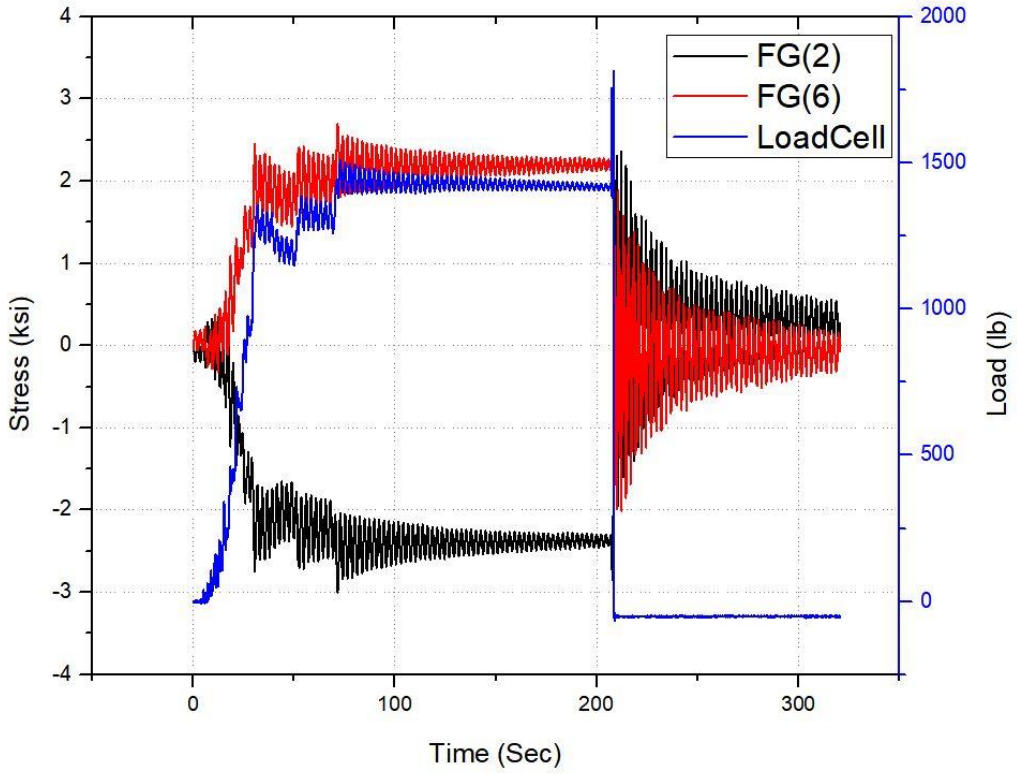

Figure 22. Sample pluck test data captured for the Baxter Interchange HMLT.

Figure 23 shows two Subfigures; Subfigure A is a sample of acceleration data collected during the Dwyer Junction pluck test. The vertical axis is acceleration in units of gravitational acceleration, *g*, and the horizontal axis is time in units of seconds. The maximum acceleration occurs at the time of load release and then dampens out toward zero. This section of the data has been highlighted in a yellow box. The data captured within the yellow box was used to perform a Fast Fourier's Transform calculation, the results of which are plotted in Subfigure B in the frequency domain. Along the vertical axis is amplitude and along the horizontal axis is frequency in units of hertz. Peak selecting was used from Subfigure B to identify the modal frequencies of each HMLT. This process was repeated using stress data for each location, as well, with natural frequencies identified up to and including mode 4. Table 2 summarizes the results of the modal frequency analysis. The results were consistent with data for other WYDOT HMLTs reported in NCHRP Report 718 (Connor et al., 2012).

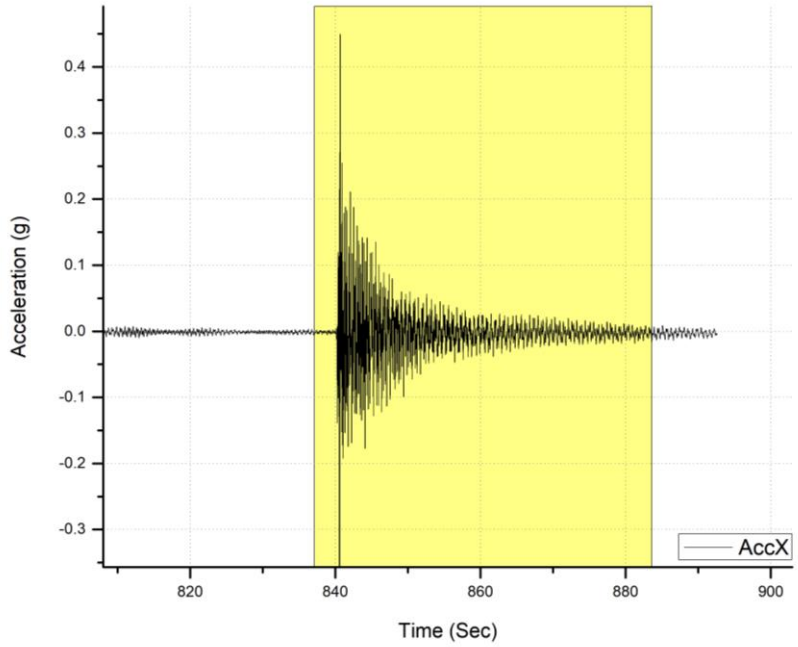

A. Subfigure example of accelerometer data used to perform the FFT plotted in Subfigure B.

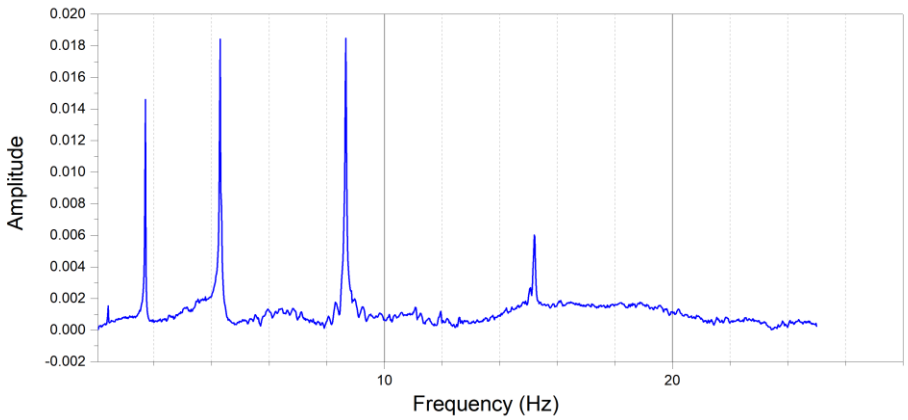

B. Subfigure example of FFT method applied to the data shown in Subfigure A.

Figure 23. Sample of pluck data from Dwyer Junction

Table 2. Modal Frequency Summary

	Using Acceleration Data				Using Strain Data			
Location	**1st**	**2nd**	**3rd**	**4th**	**1st**	**2nd**	**3rd**	**4th**
Baxter Int.	0.40	1.71	4.30	8.31	0.40	1.70	4.29	8.31
Buffalo Tri-Level	0.39	1.66	4.09	8.30	0.39	1.67	4.09	8.34
Dwyer Jct.	0.41	1.69	4.29	8.66	0.40	1.70	4.31	8.45
Vedauwoo Int.	0.39	1.57	3.93	7.69	0.38	1.58	3.93	7.69

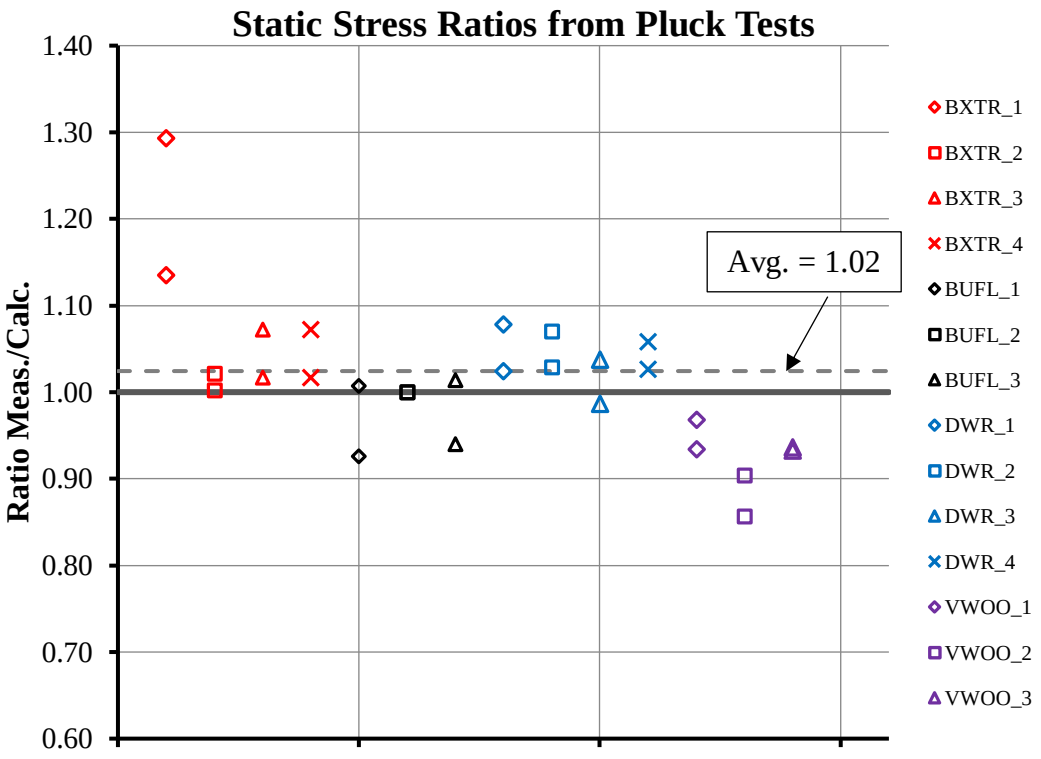

Figure 24. Summaries of Ratios of Measured to Calculated Static Stress

The pluck test data were also compared to hand calculations to further validate accuracy of the stress measurements and verify that the DAQ system was working as needed moving into the long-term monitoring program. Figure 24 plots the results of that comparison in ratios of measured to calculated stress. The hand calculation resolved the applied load into horizontal and vertical components, and accounted for the vertical portion of the load through axial stress and the horizontal portion through bending stress. Multiple pluck tests were performed for each site to ensure consistent, repeatable data. This is reflected in the figure. For each pluck test Figure 24 plots two data points. These measurements are taken from the two strain gages located at positions of maximum bending stress on opposing sides of the pole. The average ratio is

represented by the dashed line, which was 1.02. The standard deviation was 0.1 and the median value was 1.01. A possible reason for discrepancy indicated by a resulting ratio might be the assumption in the hand calculation that the load vector is truly perpendicular to the tube wall flat, when it likely was not exact despite best efforts to do so. This would change the flexural response of the pole and cause some minimal error.

Setup for the Variable Load Long-Term Monitoring

Instrumentation for the variable load long-term monitoring consisted of three primary sensors: strain gages, ice sensor, and anemometer. These sensors were installed, as described above and as detailed in Appendix A. Following completion of the pluck tests, the field team uploaded the long-term monitoring program to the data logger, and verified that communications with the modems were live and functioning properly. Then the equipment box was locked and sealed. The anemometer, ice sensor, thermocouple, strain gages, and accelerometer remained installed, now being monitored by the data logger under the long-term monitoring program.

The long-term monitoring program collected several different types of data, as defined above. Ten-minute averages and maximums were recorded under the *Ambient* data type. Once retrieved by the server at Purdue University, it was displayed for each test location on a website plotting wind direction and speeds on two wind roses, 10-minute wind maximums on a curve. An example of this website is shown in Figure 25 for the Baxter Interchange. The website also contained a tab displaying communication status and current battery bank voltage for each location as a quick check on these vital aspects of the DAQ system. In addition, wind tables were defined early in the monitoring program such that if a wind measurement was sampled above 30 mph, 40 mph, or 50 mph, the data logger would begin a trigger event sequence. This entailed recording 200 data points prior to the trigger (or about 4 seconds of continuous), and 1000 data points following the trigger event (or about 20 seconds of continuous data). After several months of collecting many 30 mph wind events, the monitoring program was adjusted to only include the 40-mph and 50-mph triggers. In addition to the wind speed triggers, peak stress triggers were also programmed such that if a stress measurement was sampled by the data logger above 5 ksi or below -5 ksi, or above 10 ksi or below -10 ksi, the data logger would initiate a trigger event sequence. In this case, similar to the wind speed triggers, the data logger would collect 200 data points leading up to the trigger and 1000, following. This means that the data logger was logging a data point from the anemometer, accelerometer, and the strain gages for the 24 seconds of triggered time-history data. Stress-based triggers were programmed for the case where low wind speeds might be able to excite large-amplitude vibrations in the pole.

In addition, the data logger was constantly monitoring output from the ice sensor. These data were sampled and stored independently of the wind and stress trigger events, but following post processing of data the Research Team was able to correlate recorded icy conditions present with the different trigger events through a synchronized time stamp, thereby enabling the team to determine any potential relationship between presence of ice and large-amplitude vibration.

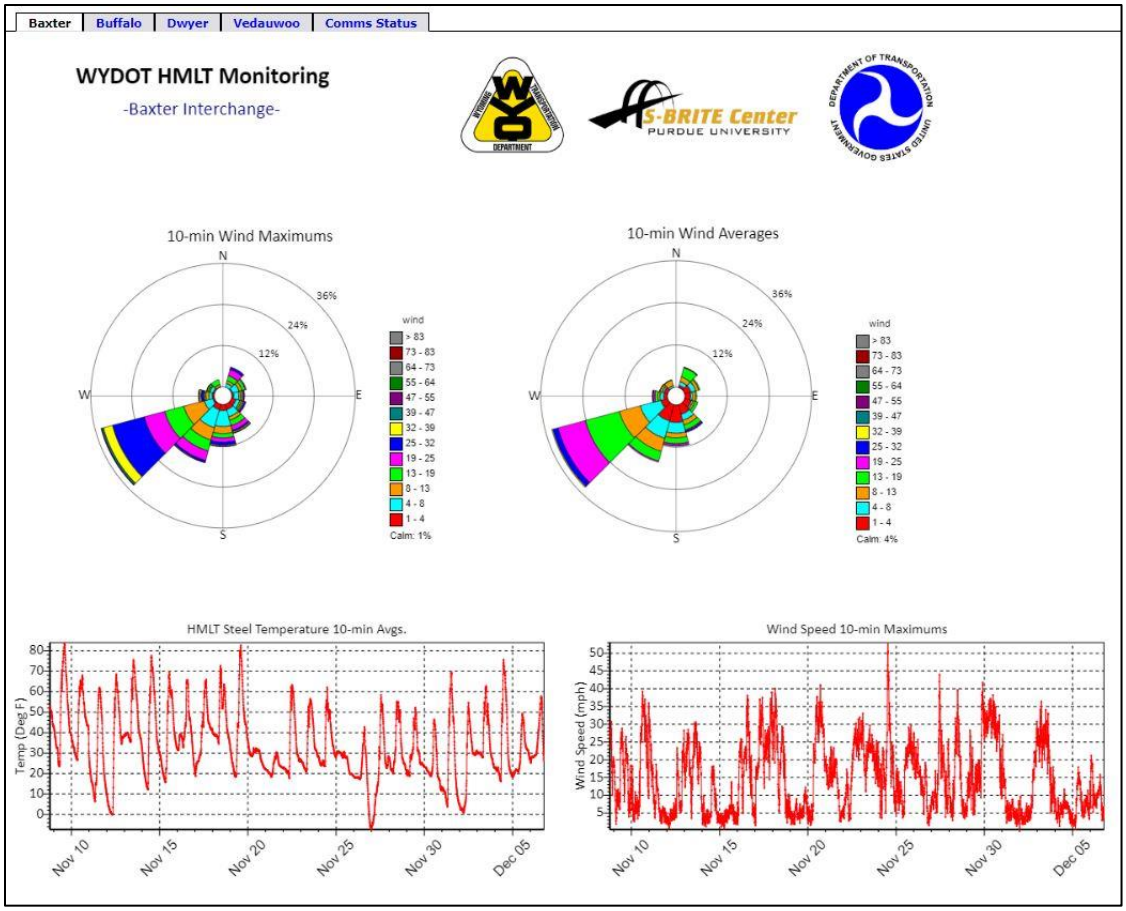

Figure 25. Web-based real time data display

Results of the Long-Term Monitoring

Based on previous field testing of HMLT's, it was known that large-amplitude mode I vibration occurrences were rare. A primary objective of the present research therefore was to record this type of structural response as many times as possible in order to better understand the correlating weather patterns and magnitude of the stress ranges it could cause. Previous research by Connor et al. (2012), as well as some amateur-captured video footage, showed evidence of large-amplitude vibration events, but little was known about the conditions that might cause it the potential resulting damage.

Across-wind motion, indicating motion normal to the direction of wind, were most often observed by the Research Team. However, there were also indications of lesser frequent along-wind motion, or a movement parallel with the direction of wind due to buffeting of the pole, an example of which is pointed out in the discussion of field testing results. Across-wind vibration caused the largest stress ranges recorded throughout testing. There were three mode I lock-in events recorded during the two years of field monitoring. These are discussed in greater detail below.

Monitoring of the poles began in September 2017 and concluded in November 2019. Within this period of time, many wind-based triggers occurred along with several stress-based triggers. The

vast majority of these data presented typical behavior of the HMLTs, such as that shown in Figure 26. This figure is a double-y plot with stress plotted along the vertical left axis and wind speed along the vertical right axis. Both are plotted against the data time stamps on the horizontal axis. Two foil resistance strain gages from the Baxter Interchange HMLT are shown, representing the largest stress ranges measured in the pole during this event. FG(1) and FG(5) were located opposite each other centered on the flats that face approximately magnetic south and north, respectively. While the oscillation period and stress reversal are typical of most observed responses for all monitored HMLTs, the magnitude of the stress ranges shown here are among the larger stress ranges generally observed for typical wind-induced oscillations. Wind speed varied 23 mph between the low of 27 mph and high of 50 mph. The average wind speed over this period of time was 34 mph and the average direction was approximately 250 degrees, or heading east-northeast. No ice was reported at the time of the event. The frequency of vibration was approximately 4 cycles over 10 seconds, or 0.4 Hz, agreeing well with the mode I resonant frequency calculated for this HMLT using pluck test data. The strain gages measuring the largest stress ranges were therefore positioned along an axis perpendicular to the direction of wind, meaning that the oscillations were across-wind. This was the most common type of motion observed throughout testing, including the largest recorded event discussed later.

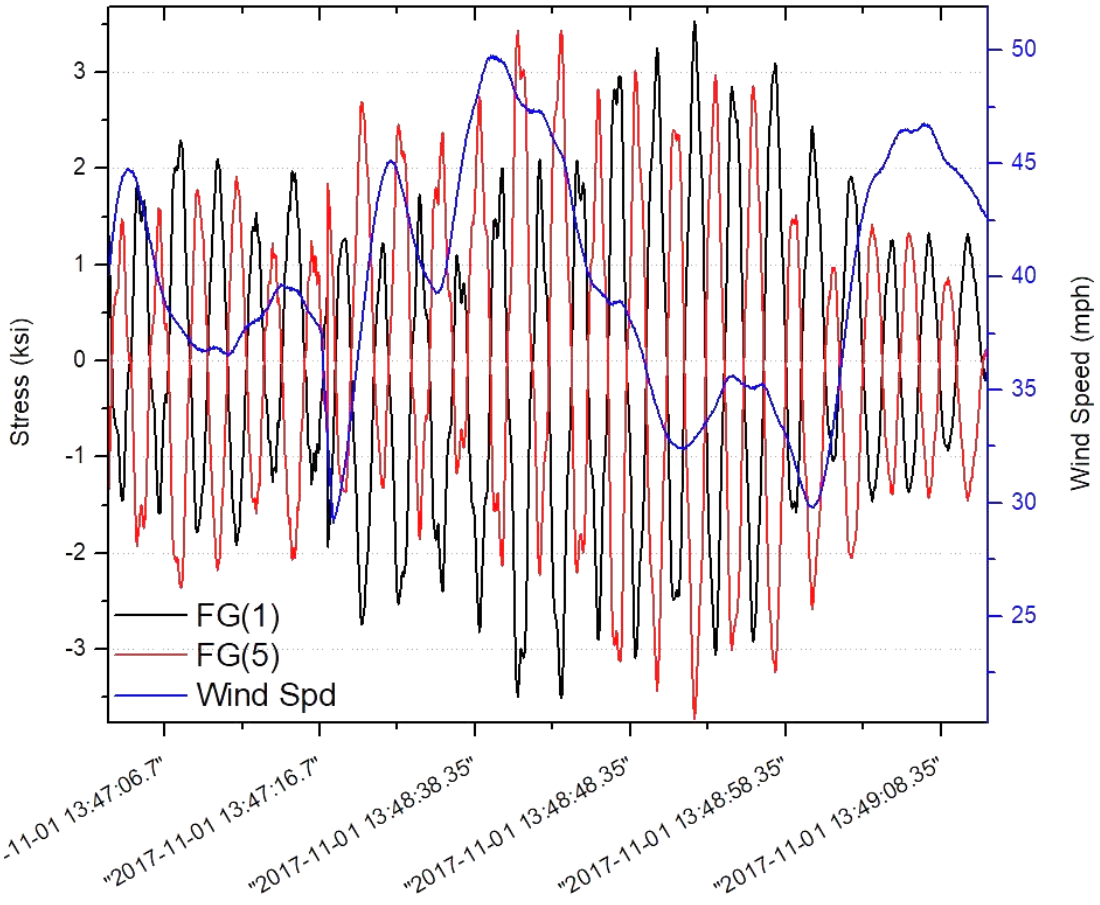

Figure 26. Data set from Baxter Interchange representing typical across-wind response

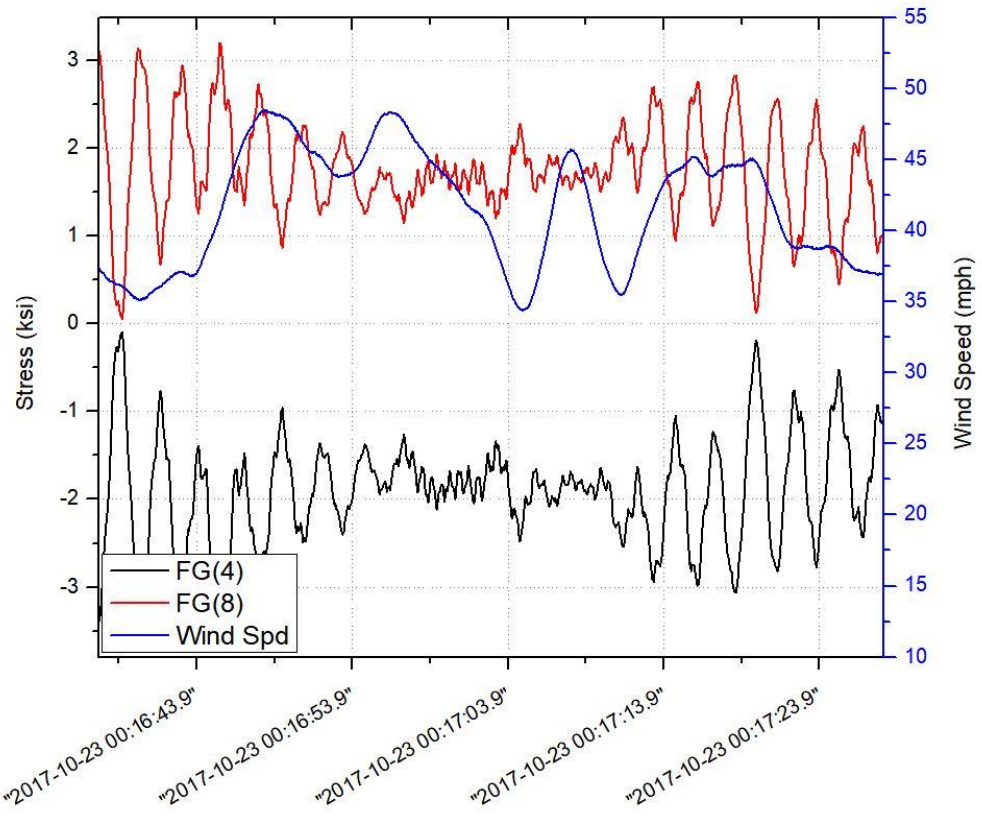

Figure 27. Data set from Buffalo Tri-Level representing typical along-wind response

Figure 27 displays a data set from the HMLT located at Buffalo Tri-level Interchange that was initiated by a Wind-40 trigger. This figure is a double-y plot with stress plotted along the vertical left axis and wind speed along the vertical right axis. Both are plotted against the data time stamps on the horizontal axis. The data from two foil resistance strain gages are shown, representing the largest stress ranges measured in the pole during this event. FG(4) and FG(8) were located opposite each other centered on the flats that face approximately magnetic northwest and southwest, respectively. Wind speed varied 12 mph between the low of 35 mph and high of 47 mph. The average wind speed over this period of time was 42.5 mph and the average direction was approximately 355 degrees, or effective heading south. No ice was reported at the time of the event. The frequency of vibration was again a mode I resonance matching measure frequencies from the pluck test.

The strain gages measuring the largest stress ranges were therefore positioned along an axis parallel to the direction of wind, meaning that the oscillations were along-wind. The stress ranges typically were smaller; in this case the largest is approximately 3.2 ksi. And as can be seen in the figure, FG(8) only measured tensile stress and FG(4) only measured compressive stress for this event, indicating that the pole was being bent in the same direction as the wind heading such that it was a buffeting wind that pushed the HMLT parallel to its path while inducing smaller amplitude vibrations. Although along-wind response was not uncommon, it was rarer than across-wind vibrations. The deflection from the event plotted in Figure 27 would have been mostly unperceivable to the eye: taking the mean stress of each gage of about 1.5 ksi results in a

calculated tip displacement of approximately 4 inches with vibrations resulting in another ±3 – 5 inches.

In addition to wind-based triggers, two stress-based triggers were programmed, as discussed above; one for ±5 ksi and the other for ±10 ksi. This was done to ensure that large stress range events would be recorded if the wind speeds which caused it were less than 30 mph (or later in testing, less than 40 mph). Figure 28 shows a Stress-5 trigger event, meaning at least one of the strain gages measured a stress of greater than 5 ksi or less than -5 ksi. The event occurred at the Vedauwoo Interchange HMLT. This figure is a double-y plot with stress plotted along the vertical left axis and wind speed along the vertical right axis. Both are plotted against the data time stamps on the horizontal axis. The data from two foil resistance strain gages are shown, representing the largest stress ranges measured in the pole during this event. FG(1) and FG(5) were located opposite each other centered on the flats that face approximately magnetic north and south, respectively. Wind speed varied 12 mph between the low of 23 mph and high of 37 mph. The average wind speed over this period of time was 31 mph and the average direction was about 290 degrees, or heading east-southeast.

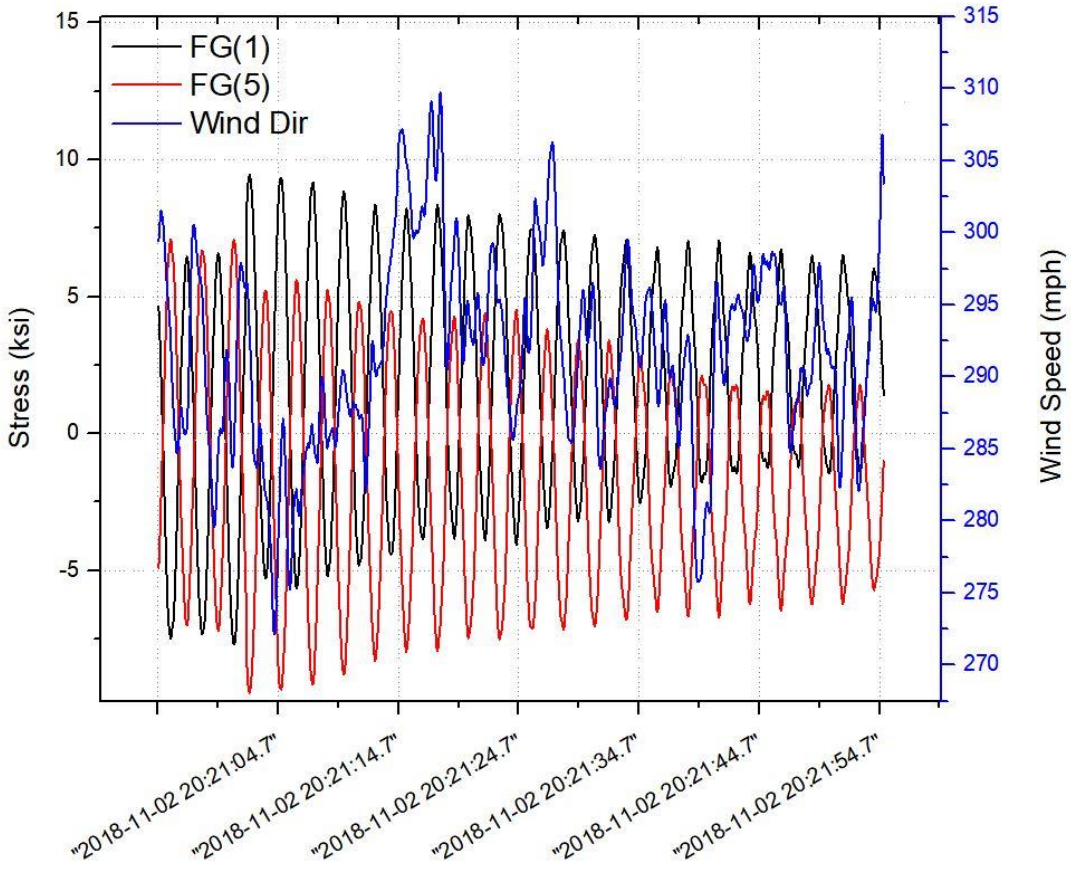

Figure 28. Data set from Vedauwoo Interchange captured on a Stress-5 trigger

The peak stress range measured during this event was 17 ksi. There was no ice reported at that time. Direction of oscillation was across-wind. The vibration frequency was close to 4 cycles over 10 seconds, or approximately 0.4 Hz. This frequency corresponded well with the calculated

mode I resonant frequency for Vedauwoo, found to be 0.39 Hz, as reported in Table 2. As can be seen on the figure, the oscillations resulted in complete stress reversal indicating smooth, large-amplitude tip displacements. A calculation of tip displacement for the 17 ksi stress range is approximately ±24 inches (or a full range of motion of 48 inches). The event was recorded on a trigger that recorded 10 seconds of data prior to the trigger, which is why the large stress cycles appear to abruptly start. Most likely there were several cycles building up to what is shown in the figure.

The event plotted in Figure 28 had similar wind characteristics to the event shown in Figure 29. Both events occurred at the Vedauwoo Interchange HMLT. In the case shown in Figure 29, the wind speed varied slightly more, 20 mph, between a low of 25 mph and high of 45 mph. The average wind speed over this period of time was 33 mph and the average direction was also 290 degrees, or heading east-southeast. However, the response of the HMLT is noticeably different, particularly in the magnitude of the stress ranges. The frequency of vibration was again the mode I resonant frequency of about 0.4 Hz and the motion was across-wind. There was no ice reported for the day of the event plotted in Figure 29, which would not necessarily be expected for August. The aerodynamic response was typical to most wind events for all of the monitored HMLTs throughout the two years of testing. Why the response plotted in Figure 28 was more significant in terms of amplitude of stress and tip displacement is inconclusive. It could be as simple as the characteristics of the wind flow were just different enough to excite lock-in phenomena in the November event (Figure 28). The presence of ice on the HMLT is also a possible explanation, particularly because the measured wind characteristics between the two events were remarkably similar.

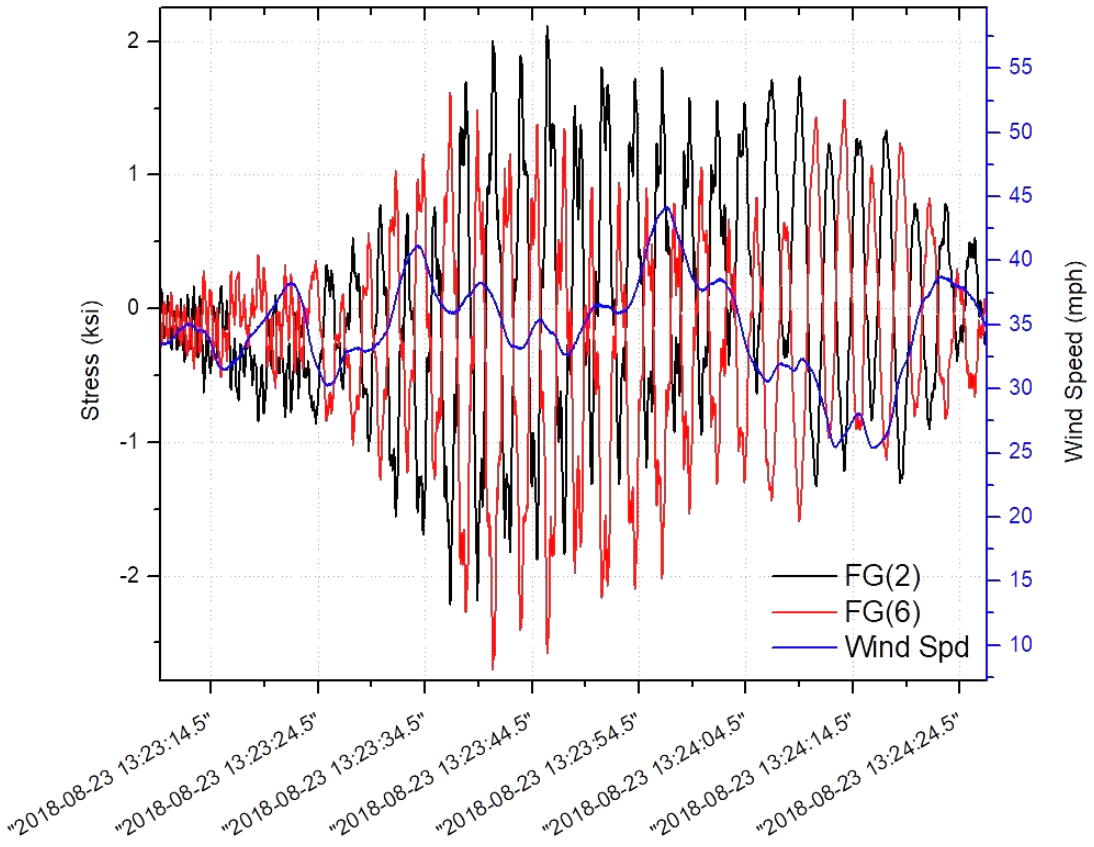

Figure 29. Data set from Vedauwoo Interchange captured on a Wind-40 trigger

Two additional large-amplitude events were recorded in the two years of monitoring. Both of them occurred at the Dwyer Junction location. The first event was initiated on a Wind-50 trigger, and is plotted in Figure 30. This figure is a double-y plot with stress plotted along the vertical left axis and wind speed along the vertical right axis. Both are plotted against the data time stamps on the horizontal axis. The data from two foil resistance strain gages are shown, representing the largest stress ranges measured in the pole during this event. FG(2) and FG(6) were located opposite each other centered on the flats that face approximately magnetic north-northeast and south-southwest, respectively. Wind speed varied 27 mph between the low of 31 mph and high of 58 mph. The average wind speed over this period of time was 37 mph and the average direction was about 280 degrees, or effectively heading east. The vibration was across-wind motion with approximately 4 cycles over 10 seconds, or 0.4 Hz. This frequency matches the calculated mode I resonant frequency for Dwyer Junction., found to be 0.4 Hz, as reported in Table 2. A calculation of tip displacement for the 32 ksi peak stress range is approximately ±41 inches (or a full range of motion of 82 inches).

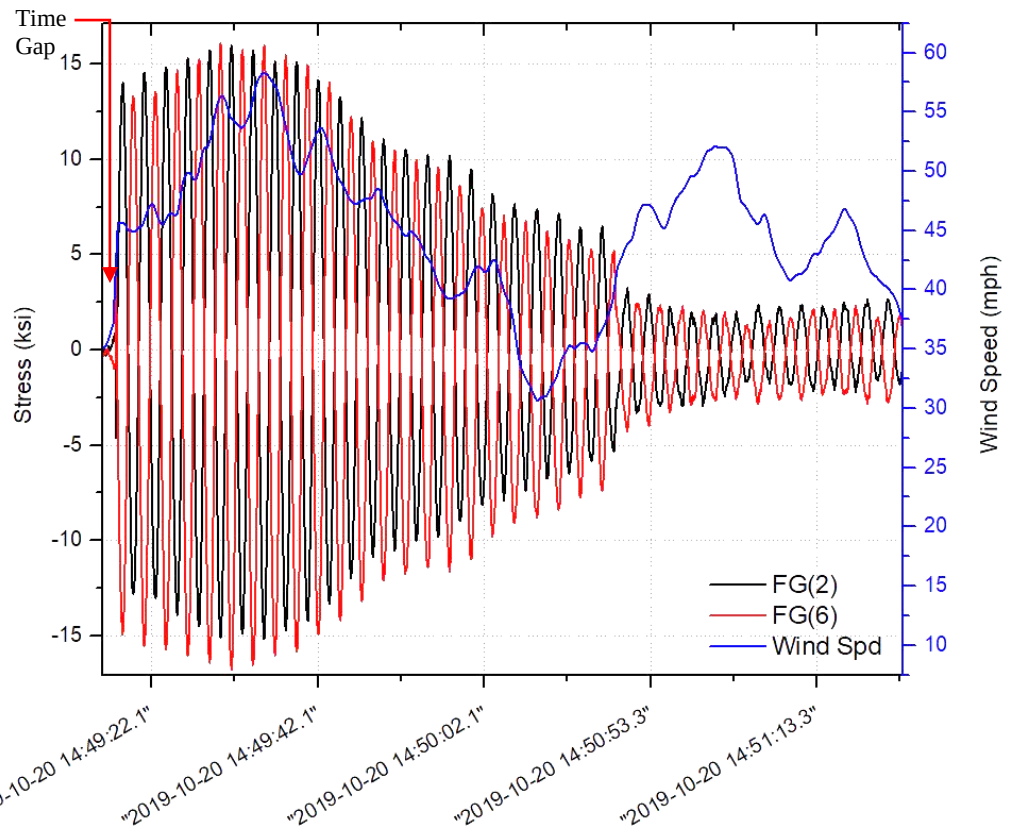

Figure 30. Large oscillation data set from Dwyer Junction captured on a Wind-50 trigger

The large amplitude cycles appear to abruptly initiate at about 1:49 p.m. It's important to keep in mind that the data logger records each event in chronological sequence, such that the data file appears to be continuous when plotted. However, a closer review of the time stamp reveals that there is a gap in time that occurs between the small stress measurements appearing at the beginning of the plot, and the large stress cycles. The large-amplitude event was captured by a Wind-50 trigger that, once the wind speed exceeded 50 mph, data for 10 sec prior to the trigger were recorded. In this case it most likely missed a few initial cycles that would have shown a buildup of stress range magnitude. The largest of the stress cycles lasted a little over 10 seconds before beginning to dampen. The entire recorded event lasted about 1 minute and 20 seconds. Note, ice was reported at 1:40 p.m., or approximately 9 minutes prior to the beginning of the recorded event, suggesting that ice was likely accumulated on the HMLT when the trigger event occurred.

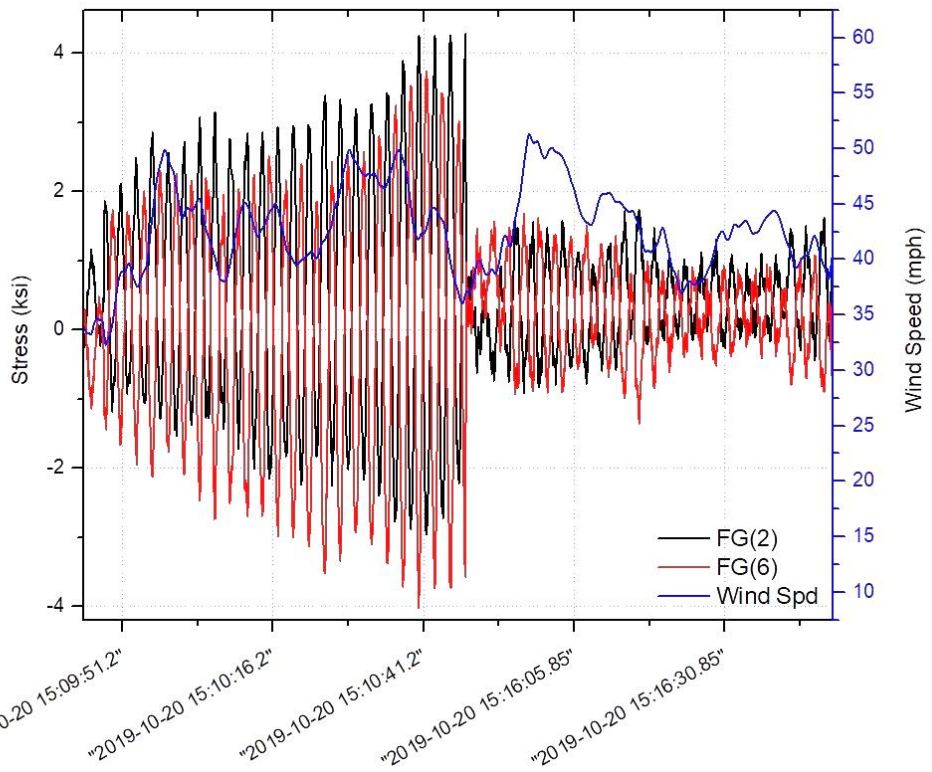

Figure 31. Data set from Dwyer Junction captured on a Wind-50 trigger

Another wind-50 trigger event for Dwyer Junction is plotted in Figure 31, which occurred just minutes after that shown in Figure 30. This figure is a double-y plot with stress plotted along the vertical left axis and wind speed along the vertical right axis. Both are plotted against the data time stamps on the horizontal axis. The data from two foil resistance strain gages are shown, representing the largest stress ranges measured in the pole during this event. FG(2) and FG(6) were located opposite each other centered on the flats that face approximately magnetic north-northeast and south-southwest, respectively. Wind speed varied 19 mph between the low of 32 mph and high of 51 mph. The average wind speed over this period of time was 40 mph and the average direction was approximately 285 degrees, or effectively heading east. The vibration was across-wind motion 0.4 Hz. A calculation of tip displacement for the 7 ksi peak stress range is approximately ±9 inches (or a full range of motion of about 18 inches).

This triggered stress time-history event demonstrates similar wind characteristics to that shown in Figure 30. It also occurred just minutes after it, therefore having the same ice accumulation still present on the pole. Thus, unlike the Vedauwoo events compared above, the data from these two Dwyer Junction events are effectively identical. However, one case resulted in an 82 inch peak tip displacement and the other resulted in less than one quarter of that. The data does not support any definitive conclusions as to why this would be the case, leaving an element of randomness to the behavior of the HMLT.

The final triggered event to be discussed herein contained the largest amplitude oscillations observed throughout monitoring. The event was initiated on a Wind-40 trigger and is plotted in

Figure 32. This figure plots stress along the vertical left axis against the data time stamps on the horizontal axis. Due to the density of the data shown, data from only a single foil resistance strain gage, FG(2), is shown representing the largest stress ranges measured in the pole during this event. FG(2) was installed on the flat that faces approximately magnetic north-northeast. The wind speed has also not been included in Figure 32 in an effort to clarify the densely plotted data. However, the 10-minute average wind speed for the entire event has been provided in Figure 33. Wind speed varied 26 mph between the low of 26 mph and high of 52 mph. As can be seen in Figure 33, the average wind speed over this period of time was between 28 and 37 mph, and the average direction was approximately 300 degrees, or a heading of east-southeast. The vibration was across-wind motion at approximately 0.4 Hz, which matches the calculated mode I resonant frequency for Dwyer Jct., as reported in Table 2. A calculation of tip displacement for the 78 ksi peak stress range totals approximately ±108 inches (or a full range of motion of 216 inches, which is equal to 18 ft.). The event appears to begin abruptly at 5:15 p.m., however, a closer review of the time stamps for the recorded data indicates an 18-min gap in time between the small stress cycles seen at the beginning of the timeline and the group of 50-60 ksi stress range cycles. This suggests that winds below 40 mph most likely initiated the dynamic response in the HMLT prior to the Wind-40 trigger that occurred around 5:15 p.m. The event continued for another 25 minutes slowly damping out around 5:40 p.m. Several small chronological gaps in the data are marked on Figure 32. This is due to the parameters of the trigger programmed into the data logger combined with the frequency of 40 mph gust occurrences. As the event continued, the data logger would complete the required number of records for a single event before a logic test on buffered data sampling could trigger recording again. Thus, if the time that elapsed between the completion of a trigger record and a new trigger (i.e., another wind speed measurement greater than or equal to 40 mph) exceeded 10 seconds, a gap in the time line would occur. This does not result in a significant loss of information, but is provided to the reader for comprehensive understanding of what is presented in Figure 32. The 18-min gap at the beginning of the triggered event prevents conclusively determining the total length of the large-amplitude vibrations, but it can be said that it lasted between 25 and 43 minutes. This means the HMLT experienced between 600 and 1,030 large amplitude cycles producing peak stresses as much as 80 percent of the yield strength of the base metal and stress ranges exceeding the yield strength by more than 50 percent.

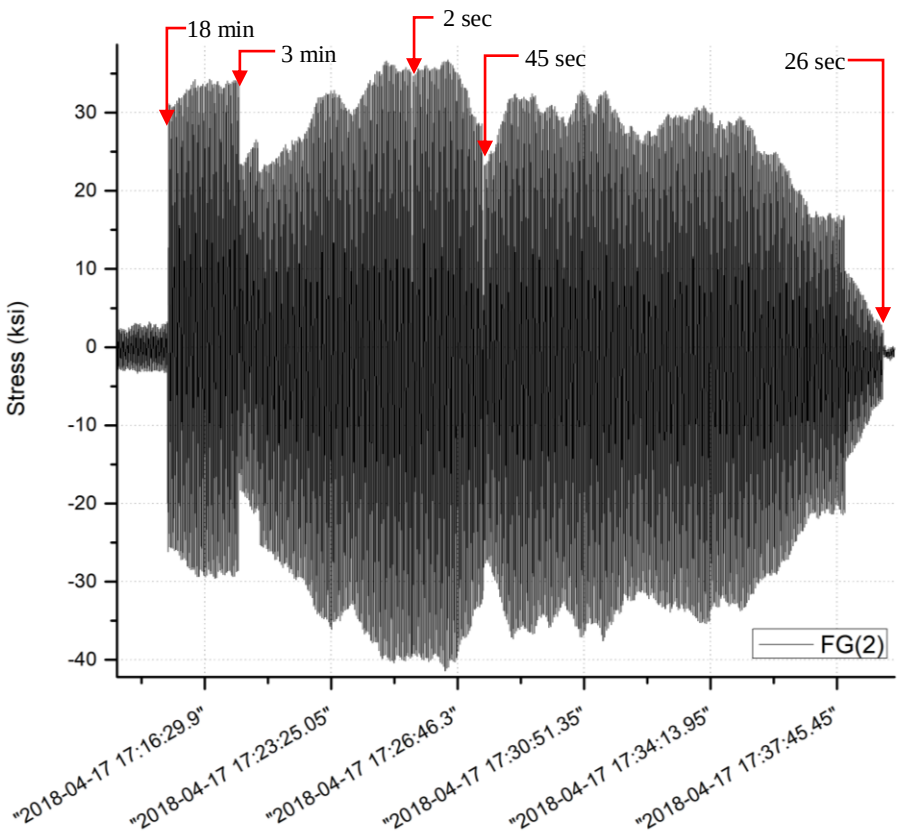

Figure 32. Large oscillation data set for Dwyer Junction captured a Wind-40 trigger

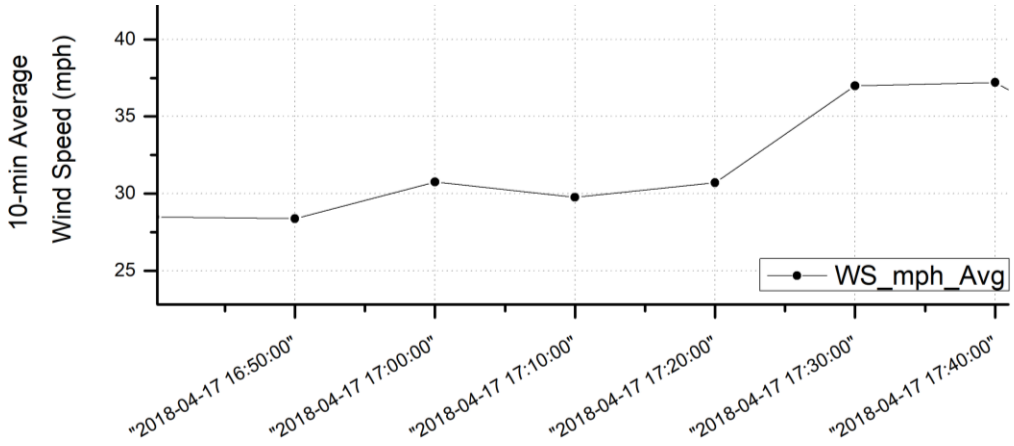

Figure 33. Ten minute interval wind speed average during large oscillation event

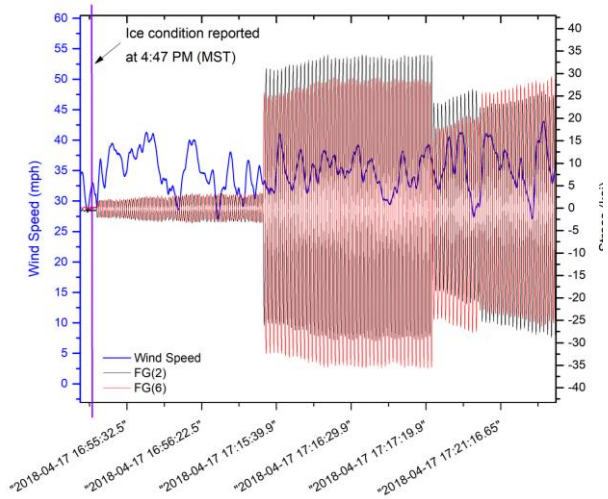

A. Subfigure showing point when ice was reported before large-amplitude event, initial cycles, and data between 4:55PM and 5:21PM

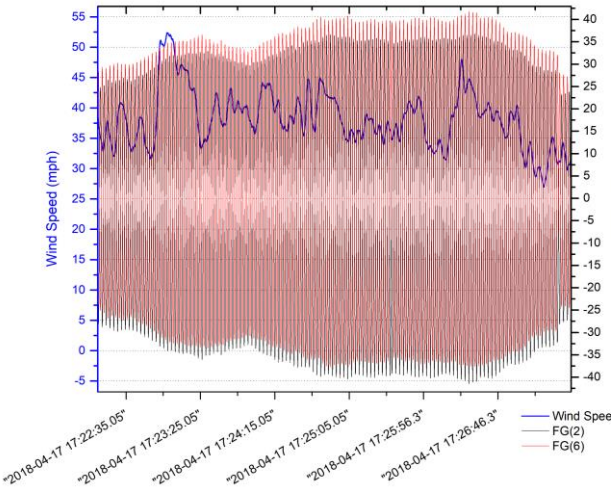

B. Subfigure continuing the stress and wind speed time-histories from 5:22PM to 5:26PM

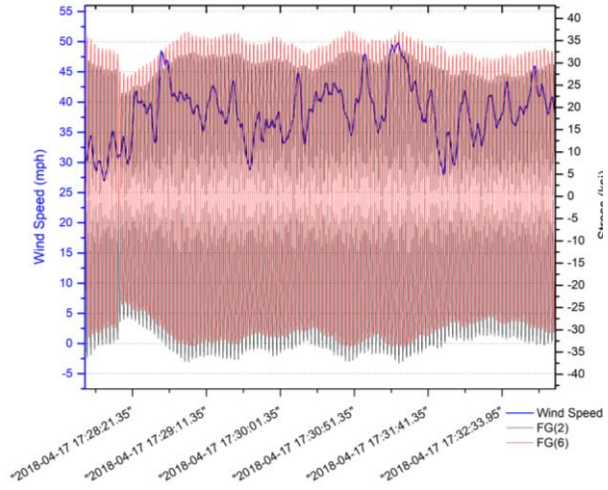

C. Subfigure continuing the stress and wind speed time histories from 5:27PM to 5:32PM

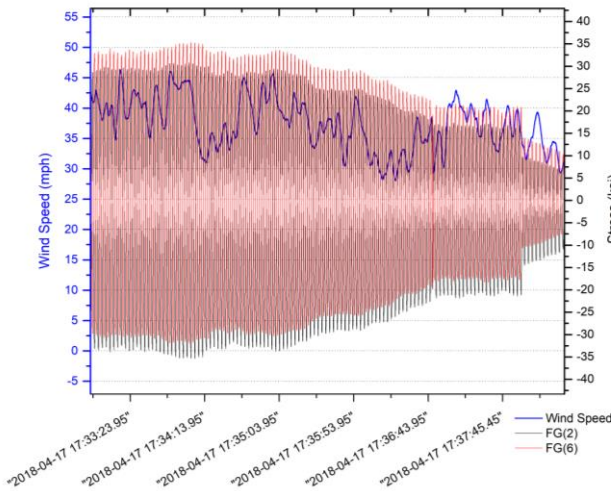

D. Subfigure continuing the stress and wind speed time histories from 5:33PM to 5:38PM

Figure 34. Data set with wind speed for large oscillation event at Dwyer Junction

Figure 34 scales up the same data shown in Figure 32 to provide some additional detail. The wind speed data has also been plotted over the stress time-history data to show how wind speed was correlated to the aerodynamic response of the HMLT. Stress ranges varied for the approximately 40 minutes of time from as high as 78 ksi to a low of about 9 ksi as the vibrations tapered off. Wind speed also varied within a range of about 30 mph to 50 mph. Finally, subfigure A shows the point in the timeline at which ice was reported, which was somewhere between 10 and 25 min prior to the start of large-amplitude vibrations.

Figure 35 zooms into the segment of largest recorded stress range cycles from the lock-in event at Dwyer Junction. It plots stress measurements from strain gages FG(2) and FG(6) on the right side vertical axis, against the time stamp along the horizontal axis. The left side vertical axis plots wind speed for the same period of time. Lock-in phenomena can be observed in the extreme magnitude of the stress ranges during which the pole was subjected to large-amplitude reversal displacements in mode I resonance (or at a frequency of 0.4 Hz). While Figure 34 indicates notable wind speed variability, smaller segments of time, such as shown in Figure 35, reveal that the wind speed remained relatively constant over sufficient periods of time to drive the structural oscillation.

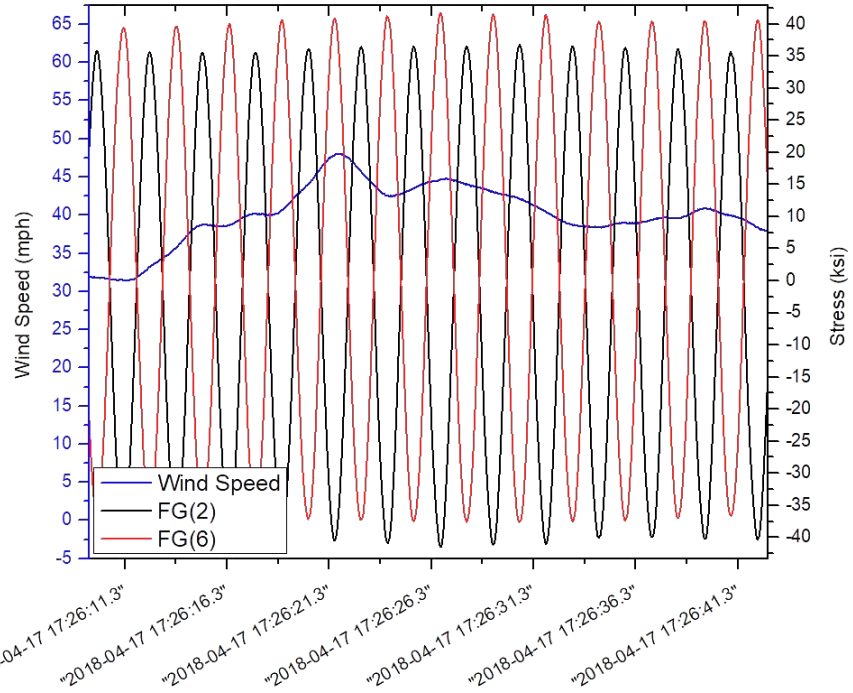

Figure 35. Thirty-second data set showing lock-in phenomena at Dwyer Jct.

Figure 36 is provided to show further detail of the observed stress measurements, adding all eight strain gages to the plot. This is a single y-axis plot with stress in units of ksi plotted along the vertical axis and data timestamps plotted along the horizontal axis. Two primary observations to be made here are that FG(2) and FG(6) measured the largest of the stress range measurements, reflecting symmetric equal-and-opposite behavior in the pole. The other supports the first, which is that gages FG(4) and FG(8) were measuring stress near zero, indicating their position would have been relatively close to the neutral axis of bending in the HMLT. The peak stress ranges observed were about 78 ksi during this period of time plotted here. FG(4) and FG(8) measured ±3 ksi. Furthermore, it can be noted that when FG(2) measured compressive stress, FG(6) measured equal magnitude and opposite sign tensile stress, and vice versa. These two strain gages were installed on the HMLT at opposite flats. This can be seen in Figure 37, where a cross section of the HMLT is provided indicating the location of each strain gage and the gage ID. In this case, “CH_2” signifies “Channel 2”, or FG(2). The same symmetry can be seen for all gages positioned opposite each other.

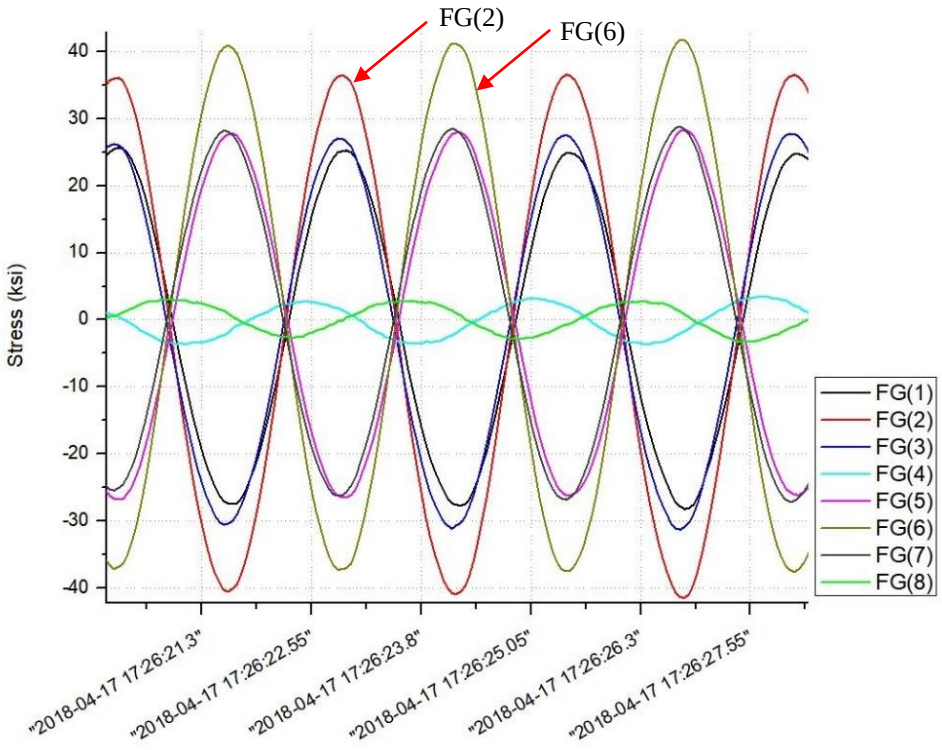

Figure 36. Close view of lock-in phenomena recorded for Dwyer Junction

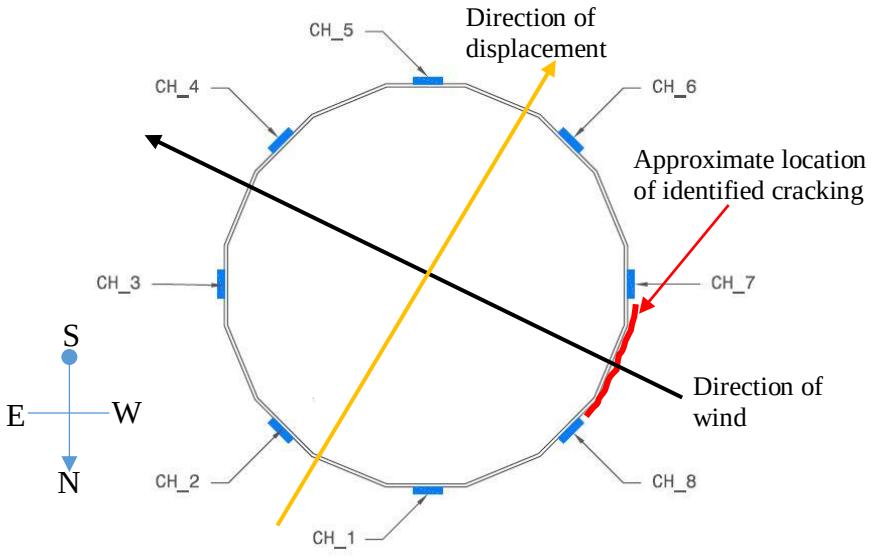

Figure 37. Planview diagram of the Dwyer Jct HMLT with cracking identified by WYDOT

Since the peak stress range measurements observed during the event were consistently seen for FG(2) and FG(6), it can be said that the direction of displacement did not vary significantly. It also indicates that the pole was displacing along the approximate axis between these two strain

gages, as labeled in Figure 37 with the golden arrow. The arrow is meant only to approximate the direction of motion of the pole. It is not drawn perfectly along the axis of FG(2) and FG(6) because stress measurements in FG(4) and FG(8) were not exactly zero, suggesting the axis of bending was close to, but not exactly along that axis. Wind direction has also been labeled on the figure using a black arrow, which was taken from wind direction data recorded from the anemometer during the event. Wind direction varied up and down a few degrees, remaining relatively consistent out of the west-northwest direction (or approximately 300 degrees). The wind direction corresponded with the peak stress measurements in FG(2) and FG(6) for cross-wind vibration.

Results of the Fatigue Life Evaluation

Data gathered during the long-term monitoring were used to perform a fatigue life analysis for each HMLT. The fatigue evaluation was performed using the AASHTO nominal stress approach for the tube wall-to-base plate weld detail using the measured stress, taken at seven feet above the base plate. Then an extrapolation factor was calculated for the nominal stress at the base plate weld. This was performed using mechanics equations found in *Deflections and Stresses in Circular Tapered Beams and Poles* by William McCutcheon (1983). The extrapolation factor used to convert the measured stress at seven feet above the base plate to the nominal stress at the base of the HMLT was 1.06 (or a 6 percent increase). The extrapolation factor was applied to the average bin stress range amplifying the effective stress range calculation for the base plate weld detail.

Rainflow cycle counting was used to create stress range histograms for the eight strain gages included in the monitoring of the weld detail. Applying a mathematical cumulative damage model called Miner's Rule to the stress-range histograms, the effective stress range was calculated for the base plate weld detail associated with each strain gage locale. The effective stress range is commonly used as a constant stress range value to compute the expected fatigue life for a variable stress range record. Equation (4) is the equation used to calculate the effective stress range; where S_{reff} is the effective stress range, $f_i = N_i/N$, N_i is the number of cycles for the specific stress range bin, N is the accumulated total number of cycles for all stress range bins, and S_{ri} is the stress range for the specific stress range bin. Knowing the effective constant amplitude stress range, the fatigue life was calculated for each of the long-term monitoring strain gage locations.

$$S_{reff} = \sum \left(f_i * {S_{ri}}^3 \right)^{1/3} \quad (4)$$

Prior to presenting the results from the fatigue evaluation it is important to briefly discuss how the data were analyzed. The data logger used for the study was capable of creating histograms based on the Rainflow cycle counting method. The stress-range histograms were created with all bins equally sized at 0.5 ksi. This was true except for the first bin, which excluded all cycles less than 0.25 ksi (i.e., the first bin ranged from 0.25 ksi to 0.5 ksi). The data logger was programmed to perform the Rainflow cycle count algorithm once every ten minutes and place all load cycles in their respective bins for each channel, for that period of time. For example, if channel 1 measured a single load cycle ranging 1.4 ksi in a given 10 minute interval, the data logger would record 1 cycle in the 1.5 ksi bin. This would be done because the 1.5 ksi bin includes all cycles

between 1 ksi and 1.5 ksi, with an average of 1.25 ksi. This process is iterated every ten minutes building the histograms used to evaluate remaining fatigue life, the results of which are summarized in Table 3. The individual stress range histograms for each HMLT are provided in Appendix B.

Once the final histograms were compiled for each strain gage (i.e., at the completion of the monitoring), a truncation was performed based on the AASHTO fatigue category appropriate for the structure detail being monitored. The truncation disregarded all cycles below a given bin. Disregarding the lower bins of a histogram is a common practice in a fatigue analysis. This is typically done so the effective stress range is not artificially reduced by the high number of very small stress range cycles, often attributed to signal "noise". A cutoff value that corresponds to between 1/4 and 1/3 of the constant amplitude fatigue limit (CAFL) of a detail is commonly used. In the case of the present research, a Category E' detail with a CAFL of 2.6 ksi was truncated such that all cycles less than 0.75 ksi were omitted. Following truncation, the effective stress range for each strain gage was then calculated using Palmgren Miner's Rule. It is noted that when calculating the effective stress range the average stress range for the bin was used. The fatigue life, as seen in Equation (5), is a function of the effective stress range. Truncating raised the effective stress range estimate, which in turn slightly reduced estimated fatigue life.

Fatigue life estimates were made for each of the strain gage locations in this study using the effective stress range and truncated histograms. Based on detail category and the truncated histogram of each strain gage, the percent of cycles exceeding the CAFL was also computed. If the number of cycles exceeding the CAFL was less than 1:10,000 (0.01 percent), the detail was determined to have infinite fatigue life. However, if more than 1:10,000 cycles exceeded the CAFL, the detail was determined to have finite fatigue life. Finite fatigue life, N_f, was computed by dividing the detail constant, A, for a given fatigue category by the detail's cubed effective stress range, S_{reff}, as shown in Equation (5).

$$N_f = \frac{A}{{S_{reff}}^3} \tag{5}$$

Next, the difference between the total fatigue life, N_f, and the amount of fatigue life used to date (structure's age), N_{used}, was computed revealing the amount of remaining fatigue life, N_r, as shown in Equation (6). The HMLT date on the construction plans for each site was used to calculate the remaining fatigue life at the time of the report.

$$N_r = N_f - N_{used} \tag{6}$$

One final important note is that fatigue life estimates (of existing structures) can range anywhere from negative years (i.e., the amount of used fatigue life is greater than the available fatigue life) up to thousands of years. Since no one can accurately predict what will happen to a structure in 100 years, let alone over 1000 years, one of three conclusions is expressed for the remaining fatigue life of a given detail: numerical between 0 and 100 years, > 100 years, or infinite. Infinite life applies to locations where the detail CAFL was not exceeded more than 0.01 percent (1/10,000). A brief summary of the fatigue life analysis results are provided in Table 3. The complete stress range histograms and fatigue life calculations are provided in greater detail in Appendix B. Note, however, that the histogram tables go up to a stress range of 16 ksi, which

means that the large amplitude events producing stress ranges in excess of 16 ksi would not be captured in this data. This is the case for Dwyer Junction. Thus, the fatigue life evaluation summarized in Table 3 does not capture the accumulated damage resulting from the April 2018 or the October 2019 lock-in events. These are evaluated separately and discussed below.

Table 3. Summary of Fatigue Life Evaluations

Truncation		**0.375 ksi**		**0.75 ksi**			
Location	**Gage ID**	S_{reff}	**% Exceedance**	S_{reff}	**% Exceedance**	**Cycles/ Day**	**Remaining Life**
Baxter Int.	FG(3)	1.1	0.98	1.7	4.5	1270	> 100
Buffalo Tri-Level	FG(4)	1.1	0.61	1.6	3.3	603	> 100
Dwyer Jct.*	FG(6)	1.0	0.27	1.6	2.0	991	> 100
Vedauwoo Int.	FG(6)	1.2	2.22	1.8	8.3	14,785	-2.5

*Note: This fatigue life evaluation does not include accumulated fatigue damage resulting from the April 2018 and October 2019 large-amplitude stress range events and therefore does not accurately reflect the actual remaining fatigue life.

A separate fatigue analysis was performed specifically for the large-amplitude event recorded for Dwyer Junction discussed above. It was separated out specifically to understand what effect a large-amplitude lock-in event would have on the fatigue life. The data set was evaluated using the Rainflow algorithm to generate the stress range histogram and calculate the accumulated fatigue damage. The same extrapolation factor was used to calculate the nominal stress ranges at the base of the HMLT. The analysis was performed assuming mechanics of linear-elastic high-cycle fatigue, ignoring the possibility for low-cycle fatigue behavior caused by the extreme stress ranges, in addition to "oil canning" effects that can incur additional stress amplification through distortion of thin walled structures. While it is possible that these factors were influencing behavior and contributing to fatigue life damage, they were not expressly investigated for their effect on the total fatigue damage incurred. Thus, the following summary of the analysis solely represents a typical AASHTO nominal stress approach using mechanics of high-cycle fatigue. Table 4 summarizes the results using data for strain gage FG(6) because this gage measured some of the largest stress ranges. The effective stress range calculated was 64.2 ksi with a 99.8 percent exceedance. Recall that percent exceedance indicates how frequently the constant amplitude fatigue limit (CAFL) was exceeded during the stress time-history data. Also, the effective stress range exceeds the nominal yield strength of the base metal of 50 ksi. Table 4 reports that the fatigue life, N_f, was found to be effectively consumed with a remaining life of 0 years. This really means that there are zero years of fatigue life available in the HMLT at this effective stress range. It does not necessarily mean that the entire fatigue life was actually used up. This has been illustrated in the SN curve plot shown in Figure 38. This figure plots two data points along with the standard log-log SN curves for the AASHTO Fatigue Category E and E' for reference. The two data points represent the calculated consumed fatigue life for a 25-min and 43-min event duration. Recall from above that due to a gap in the data file resulting from a lack of winds above 40 mph to trigger, it is not known how long the HMLT was cycling under lock-in. However, it can be said that it was sometime between 25 and 43 minutes. At the rate of natural vibration of the HMLT, or 0.4 cycles per second, it would accumulate between 600 (25-min estimate) and 1,030 cycles (43-min estimate). Thus, Figure 38 plots the 25-min data point and the 43-min estimate data point showing how much fatigue life would be consumed at the

effective stress range of 64.2 ksi for each of these cycle counts. As can be seen in the figure, the 43-min estimate of 1,030 cycles nearly approaches the design life curve for Category E'.

Note that in fatigue life evaluations, a linear accumulation of fatigue damage can be calculated for differing effective stress ranges and the percentage consumed for each available life at a given effective stress range can be computed. Thus, it can be further examined noting from Table 4 that the N_{f_Design} (or the number of cycles to reach the AASHTO design life for Category E') is 1,474 cycles. This means that the single event recorded on April 17, 2018, consumed between 41 percent (25-min estimate) and 70 percent (43-min estimate) of the design fatigue life of the base weld detail. Furthermore, it cannot be said that this was the only large-amplitude event experienced by the HMLT during its five year service life. And as shown in Table 3, the Dwyer Junction HMLT was in a finite life regime with two percent exceedance. Calculating the number of available cycles at an effective stress range of 1.6 ksi, and then dividing that that into the number of consumed cycles indicates that about two percent of the fatigue life had been consumed in those same five years by normal daily vibration. This is an insignificant amount of accumulated damage, making it clear that the fatigue cracks found in the base of the Dwyer Junction HMLT by WYDOT personnel in December 2019 must be the result of isolated large-amplitude events such as those recorded on April 17, 2018, and October 20, 2019. That said, this does not rule out the possible effect that fabrication or galvanizing defects might have. Finally, this only includes high-cycle fatigue assumptions without consideration for local tearing due to low-cycle fatigue nor thin wall distortion-induced stress range amplifications at the base of the pole that could be further increasing fatigue damage accumulation during extreme events, such as that in April 2018.

Table 4. Fatigue Life Evaluation for Dwyer Large-Amplitude Event

Truncation				**0.75 ksi**		
Location	**Gage ID**	N_{f_Design} **(Cycles)**	N_{f_Mean} **(Cycles)**	S_{reff}	**% Exceedance**	**Remaining Life**
Dwyer Jct	FG(6)	1,474	2,800	64.2	99.8	0

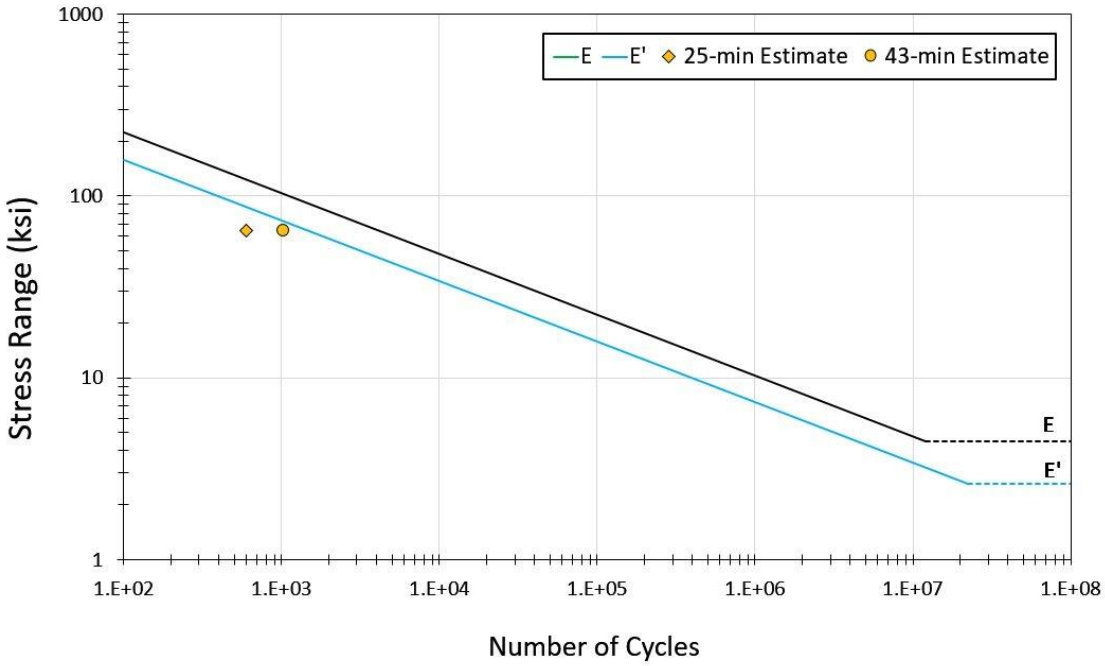

Figure 38. SN curve showing fatigue life consumed by the April 2018 large-amplitude event at Dwyer Junction

CHAPTER 4. FINDINGS, CONCLUSIONS & RECOMMENDATIONS

FINDINGS

The following conclusions are the result of a two-year study that included field monitoring of four high mast lighting towers located in Wyoming. The primary objective was to observe a rare lock-in event generating high amplitude displacements and stress ranges in one or more of the HMLTs, which prior to this study, had been observed only in amateur video by passers-by. Some limited data was also observed by Connor et al. (2012), but without conclusive evidence. Three large amplitude events were observed during the present two-year study. One event took place in November 2018, at Vedauwoo Interchange, resulting in peak stress range of about 17 ksi (42 inch calculated tip displacement range) and total duration of about 50 seconds. Another event was recorded in October 2019, at Dwyer Junction, resulting in a peak stress range of about 32 ksi (84 inch calculated tip displacement range) and total duration of about 1-1/2 minutes. And finally, the largest event was recorded at Dwyer Junction, in April 2018, resulting in a peak stress range of 78 ksi (216 inch calculated tip displacement range) and a total duration of between 25 and 43 minutes.

Prior to the present study, it was not understood what the magnitude of stress ranges might be induced in an HMLT during a large-amplitude mode I lock-in event. This has now been observed resulting in the following findings:

- During the October 2019 event, a peak stress range of 32 ksi was measured; the event resulted in a 24 ksi effective stress range.
- During the April 2018 event, a peak stress range of 78 ksi was measured; the event resulted in a 64.2 ksi effective stress range.

CONCLUSIONS

The present study further resulted in the following conclusions:

- With an effective stress range of 64.2 ksi, the Category E' fatigue detail at the pole-to-base plate weld detail is designed for about 58 min (1474 cycles) of lock-in resonant mode I vibration. The mean life for this same effective stress range is about 116 min (2800 cycles). It stands to reason, therefore, that within a few long-duration events, such as was observed at Dwyer Junction, in April 2018, the fatigue life of the base weld can be consumed. This is ignoring the possibility of low-cycle fatigue behavior, distortion-induced fatigue stress amplification, or local plastic tearing. The effect of any of these three phenomena would further reduce the fatigue life.
- Large-amplitude mode I vibration is a rare occurrence, being observed only three times while monitoring four HMLTs continuously over two years.
- Based on the observed data, it stands to reason that the entire design fatigue life of the WYDOT HMLT pole-to-base plate weld detail could be consumed in a single large-amplitude mode I vibration event.

- The average effective stress range resulting from daily vibrations under normal wind conditions was found to be 1.7 ksi.
- HMLTs not subjected to large-amplitude mode I vibration events were found to be in the finite fatigue life regime with over 100 years of remaining fatigue life.
- Ice was reported present within several minutes to an hour of two of the three large-amplitude mode I lock-in events. There were many more occasions in which ice accumulation was reported with similar wind speeds that did not result in the same lock-in response. The present study did not produce the data required to determine why one wind event resulted in lock-in and another did not. The resonant mode I vibration appears to be somewhat random; meaning that it is the pairing of the HMLT aerodynamic properties (which may be temporarily altered with ice accumulation) and the wind properties that can trigger this response. This can be interpreted to mean that the same response could be expected in an HMLT without ice, so long as the wind characteristics match the resonant frequency of the pole. Ice is not necessarily required for it to occur.
- Literature review related to galvanizing cracking suggests that HMLTs could be put into service with cracking already present, which would significantly shorten fatigue life. However, it is not conclusive as to whether or not it could be affecting fatigue performance of HMLTs in Wyoming. There is no evidence presently available for the Dwyer Junction HMLT to suggest that galvanizing cracking was present.

RECOMMENDATIONS

The following three recommendations resulted from the present study:

- Continue field monitoring of as many HMLTs as possible in an effort to capture further data during large-amplitude lock-in events. Further data would improve upon understanding of what conditions initiate the extreme structural responses and the effects these events have on the HMLTs.
- Explore options to mitigate the resonant response that results in large-amplitude structural oscillation in the HMLT to protect against the rapid fatigue damage accumulation resulting from a lock-in phenomenon.
- Future research, including experimental fatigue testing of several HMLTs subjected to stress ranges similar to that observed during the April 2018 large-amplitude event at Dwyer Junction. The large-amplitude stress ranges observed in the laboratory setting would allow researchers to determine what local behavior is occurring and what factors are contributing to fatigue damage. Following large-amplitude cycling, continue testing the HMLTs applying more typical high-cycle fatigue stress ranges to determine what the fatigue life might be following such large-amplitude cycles.

REFERENCES

Bellivanis, K. V. (2014) *Assessment of Remaining Fatigue Performance of High Mast Illumination Poles*. Master's Thesis, University of Texas at Austin.

Connor, R. J., Collicott, S. H., DeSchepper, A. M., Sherman, R. J., & Ocampo, J. A. (2012). *Development of Fatigue Loading and Design Methodology for High-Mast Light Poles*. NCHRP Report 718. Washington, DC: Transportation Research Board.

Connor, R. J., & Hodgson, I. C. (2006). Field Instrumentation, Testing, and Long-term Monitoring of High Mast Lighting Towers in the State of Iowa, TR-518. Iowa Department of Transportation.

Kleineck, J. R. (2011). *Galvanizing Crack Formation at Base Plate to Shaft Welds of High Mast Illumination Poles*. Master's Thesis, University of Texas at Austin.

Magenes, L. (2011). *Fatigue Assessment of High Mast Illumination Poles Using Field Measurements*. Master's Thesis, University of Texas at Austin.

McCutcheon, W. J. (1983). *Deflections and Stresses in Circular Tapered Beams and Poles*. Civil Engineering for Practicing and Design Engineers. 2: 207-233. US Department of Agriculture, Madison, WI.

Nasouri, R., Nguyen, K., Montoya, A., Matamoros, A., Bennett, C., and Li, J. (2019a). *Simulating the Hot Dip Galvanizing Process of High Mast Illumination Poles. Part I: Finite Element Model Development*. Journal of Construction Steel Research, Volume 162.

Nasouri, R., Nguyen, K., Montoya, A., Matamoros, A., Bennett, C., and Li, J. (2019b). *Simulating the Hot Dip Galvanizing Process of High Mast Illumination Poles. Part II: Effects of Geometric Properties and Galvanizing Practices*. Journal of Construction Steel Research, Volume 159.

Sherman, R. J., and Connor, R. J. (2019). *Development of a Fatigue Design Load for High-Mast Lighting Towers*. Journal of Structural Engineering, Volume 145, Issue 1

APPENDIX A – HMLT INTRUMENTATION PLANS

APPENDIX B – STRESS RANGE HISTOGRAM DATA

Table 5. Baxter Interchange Stress Range Histogram Data

RANGE	R_AVG	CH_1	CH_2	CH_3	CH_4	CH_5	CH_6	CH_7	CH_8
0.25	0	0	0	0	0	0	0	0	0
0.5	0.375	3127853	16678468	10266795	16730900	19275883	14943365	5717767	16172020
1	0.75	1334288	5797131	3849696	5547190	7300167	4739534	2116948	5247522
1.5	1.25	165465	696802	682693	644412	860953	501637	329202	602024
2	1.75	19668	143657	197892	116723	127252	93263	69512	113352
2.5	2.25	3357	37199	78506	27079	25631	21042	21883	25975
3	2.75	891	11036	29361	6779	6506	5471	5262	6747
3.5	3.25	287	3249	10790	1543	1872	652	774	1295
4	3.75	103	374	3901	530	676	179	494	439
4.5	4.25	38	126	958	181	267	63	37	176
5	4.75	13	48	4	85	114	21	1	111
5.5	5.25	3	19	1	29	59	23	0	86
6	5.75	5	25	0	38	35	12	0	56
6.5	6.25	2	11	0	30	29	16	0	29
7	6.75	0	14	0	17	21	27	0	35
7.5	7.25	2	24	0	26	14	18	0	12
8	7.75	2	18	0	5	25	14	0	5
8.5	8.25	1	16	0	1	23	8	0	1
9	8.75	0	10	0	0	15	18	0	0
9.5	9.25	0	13	0	0	7	19	0	0
10	9.75	0	17	0	0	11	28	0	0
10.5	10.25	0	17	0	0	15	10	0	0
11	10.75	0	24	0	0	14	10	0	2
11.5	11.25	0	6	0	0	16	13	0	0
12	11.75	0	12	0	0	8	7	0	4
12.5	12.25	0	12	0	0	20	0	0	0
13	12.75	0	6	0	0	7	0	0	1
13.5	13.25	0	1	2	0	9	4	0	0
14	13.75	0	0	0	0	9	0	0	2
14.5	14.25	0	0	4	0	1	4	0	0
15	14.75	0	0	0	0	0	0	1	1
15.5	15.25	0	0	1	0	0	1	1	0
16	15.75	0	0	0	0	0	0	0	0
S_{reff} (ksi)		**1.4**	**1.55**	**1.67**	**1.52**	**1.48**	**1.52**	**1.57**	**1.52**
% Exceedance		0.71%	1.69%	4.48%	1.16%	0.95%	1.06%	1.54%	1.20%
Remaining Life		> 100	> 100	> 100	> 100	> 100	> 100	> 100	> 100

Table 6. Buffalo Tri-Level Interchange Stress Range Histogram Data

RANGE	R_AVG	CH_1	CH_2	CH_3	CH_4	CH_5	CH_6	CH_7	CH_8
0.25	0	0	0	0	0	0	0	0	0
0.5	0.375	9747507	11601677	7090896	5681723	10194846	10344211	6920621	5103776
1	0.75	3414236	4719329	2485497	2086364	3703186	3823895	2410633	1838677
1.5	1.25	406712	549113	329537	352738	474714	365839	318676	293637
2	1.75	66290	78749	67061	81685	82011	47782	64664	63664
2.5	2.25	14789	16078	19204	24216	18993	10003	18243	18769
3	2.75	4467	4805	6683	8991	5712	2828	6549	6858
3.5	3.25	1563	1666	2944	3826	1999	1097	2809	2782
4	3.75	551	701	1197	1564	829	436	1172	1152
4.5	4.25	189	348	537	754	312	254	515	416
5	4.75	65	173	265	289	105	112	251	189
5.5	5.25	50	90	137	129	54	55	129	64
6	5.75	11	33	61	55	28	23	61	44
6.5	6.25	7	33	36	38	11	18	35	3
7	6.75	5	13	15	9	10	6	13	2
7.5	7.25	4	0	5	2	1	11	9	0
8	7.75	1	8	8	0	4	0	4	0
8.5	8.25	0	0	0	0	1	6	1	0
9	8.75	0	4	1	0	0	1	0	0
9.5	9.25	0	1	0	0	0	1	0	0
10	9.75	1	0	0	0	0	1	0	1
10.5	10.25	0	0	0	1	0	0	0	0
11	10.75	0	1	1	1	0	0	0	0
11.5	11.25	0	0	0	0	0	0	0	1
12	11.75	0	0	0	0	0	0	0	0
12.5	12.25	0	0	0	0	0	0	0	0
13	12.75	0	0	0	0	0	0	0	0
13.5	13.25	0	0	0	0	1	0	0	0
14	13.75	0	0	0	0	0	0	0	0
14.5	14.25	0	0	0	0	0	0	0	0
15	14.75	0	0	0	0	0	0	0	0
15.5	15.25	0	0	0	0	0	0	0	0
16	15.75	0	0	0	0	0	0	0	0
S_{reff} (ksi)		**1.51**	**1.48**	**1.56**	**1.59**	**1.52**	**1.47**	**1.56**	**1.58**
% Exceedance		1.40%	1.21%	2.78%	3.30%	1.55%	1.13%	2.80%	2.97%
Remaining Life		> 100	> 100	> 100	> 100	> 100	> 100	> 100	> 100

Table 7. Dwyer Junction Stress Range Histogram Data

RANGE	R_AVG	CH_1	CH_2	CH_3	CH_4	CH_5	CH_6	CH_7	CH_8
0.25	0	0	0	0	0	0	0	0	0
0.5	0.375	31982840	30748486	26314481	26728627	30057885	15806995	31520588	29662738
1	0.75	5243981	5282831	4267726	4790737	4634195	3179443	4616132	5091216
1.5	1.25	475414	579146	444650	438564	414975	384830	433546	454103
2	1.75	105101	121127	95349	90662	90390	91150	83307	93440
2.5	2.25	33059	31386	21600	26203	26852	23280	17236	27477
3	2.75	11013	8837	4956	8070	8416	6278	3514	8744
3.5	3.25	3607	2696	1315	2618	2542	1757	757	3007
4	3.75	1453	1083	652	990	961	635	192	1288
4.5	4.25	520	731	300	571	359	296	104	751
5	4.75	198	532	278	406	174	303	61	523
5.5	5.25	96	453	157	233	128	116	51	404
6	5.75	76	339	82	182	64	82	35	304
6.5	6.25	28	383	42	107	47	55	14	168
7	6.75	26	330	25	93	26	39	7	124
7.5	7.25	18	253	20	74	25	47	10	95
8	7.75	21	253	18	30	17	36	21	84
8.5	8.25	10	232	23	24	16	64	15	45
9	8.75	15	241	18	10	9	35	15	13
9.5	9.25	9	213	19	9	15	70	7	11
10	9.75	15	186	9	15	11	41	11	5
10.5	10.25	18	258	14	0	15	23	7	3
11	10.75	17	231	9	1	14	18	6	5
11.5	11.25	14	190	7	1	23	18	6	1
12	11.75	12	164	6	1	12	13	4	1
12.5	12.25	6	183	12	1	5	16	6	2
13	12.75	3	90	5	2	7	20	17	0
13.5	13.25	6	93	11	0	6	20	19	1
14	13.75	8	53	18	0	6	20	32	1
14.5	14.25	10	64	23	0	7	27	19	1
15	14.75	4	57	32	1	5	20	26	1
15.5	15.25	2	33	14	0	5	15	36	0
16	15.75	9	34	38	0	8	8	34	0
S_{reff} (ksi)		**1.59**	**1.55**	**1.54**	**1.56**	**1.57**	**1.57**	**1.51**	**1.56**
% Exceedance		2.73%	2.43%	1.42%	2.36%	2.37%	1.98%	0.93%	2.64%
Remaining Life		> 100	> 100	> 100	> 100	> 100	> 100	> 100	> 100

Table 8. Vedauwoo Interchange Stress Range Histogram Data

RANGE	R_AVG	CH_1	CH_2	CH_3	CH_4	CH_5	CH_6	CH_7	CH_8
0.25	0	0	0	0	0	0	0	0	0
0.5	0.375	78981765	5978377	78600194	80395517	83126838	82813315	86647689	65355576
1	0.75	24231722	2543288	28612023	25007677	26281333	26147699	34654245	22466405
1.5	1.25	5615901	724015	5621690	4698399	5773910	5679449	6159435	4563126
2	1.75	2104011	322377	1872272	1588902	2083549	2147915	1941228	1246037
2.5	2.25	864736	147215	647475	609170	850309	957807	690412	366288
3	2.75	373049	67416	263259	287295	381908	442714	281978	113058
3.5	3.25	152083	31112	135632	143795	201686	195757	168868	35439
4	3.75	57626	12355	72345	75520	107268	86807	134331	12255
4.5	4.25	22392	5129	29825	35636	54758	38229	103909	3213
5	4.75	8095	2157	11304	12202	26924	16083	60360	974
5.5	5.25	3055	821	4661	4625	10268	7432	25682	379
6	5.75	1323	385	2063	2004	4435	3536	9895	174
6.5	6.25	625	174	1020	1620	2127	1591	4903	104
7	6.75	311	77	555	1373	1091	784	2429	81
7.5	7.25	307	42	286	1561	684	556	1477	50
8	7.75	135	22	272	1091	405	376	786	30
8.5	8.25	134	13	143	489	189	282	499	5
9	8.75	77	10	75	392	129	220	234	0
9.5	9.25	83	4	50	228	61	182	256	0
10	9.75	41	1	70	240	53	155	164	5
10.5	10.25	42	1	35	318	28	90	93	0
11	10.75	20	0	0	328	30	104	37	0
11.5	11.25	15	0	7	155	10	78	24	0
12	11.75	30	0	0	74	30	74	49	0
12.5	12.25	17	0	0	30	20	43	27	0
13	12.75	15	0	0	90	15	32	47	0
13.5	13.25	15	0	0	75	10	19	30	0
14	13.75	25	0	0	68	25	0	47	0
14.5	14.25	15	0	0	70	15	0	18	0
15	14.75	20	0	0	57	20	0	27	0
15.5	15.25	0	0	0	21	0	5	6	0
16	15.75	0	0	0	35	0	2	8	0
S_{reff} (ksi)		**1.73**	**1.78**	**1.67**	**1.70**	**1.72**	**1.75**	**1.65**	**1.61**
% Exceedance		6.73%	9.12%	6.02%	7.63%	8.34%	8.30%	8.30%	2.61%
Remaining Life		-1.50	5.44	1.06	2.88	-1.58	-2.48	-0.03	10.14